Journal Pre-proof

Effects of asymmetric acceptor and donor positioning in deep blue pyridyl-sulfonyl based TADF emitters

Gulcin Haykir, Murat Aydemir, Andrew Danos, Selcuk Gumus, Gurkan Hizal, Andrew P. Monkman, Figen Turksoy

Please cite this article as: Haykir G, Aydemir M, Danos A, Gumus S, Hizal G, Monkman AP, Turksoy F, Effects of asymmetric acceptor and donor positioning in deep blue pyridyl-sulfonyl based TADF emitters, *Dyes and Pigments*, https://doi.org/10.1016/j.dyepig.2021.109579.

This is a PDF file of an article that has undergone enhancements after acceptance, such as the addition of a cover page and metadata, and formatting for readability, but it is not yet the definitive version of record. This version will undergo additional copyediting, typesetting and review before it is published in its final form, but we are providing this version to give early visibility of the article. Please note that, during the production process, errors may be discovered which could affect the content, and all legal disclaimers that apply to the journal pertain.
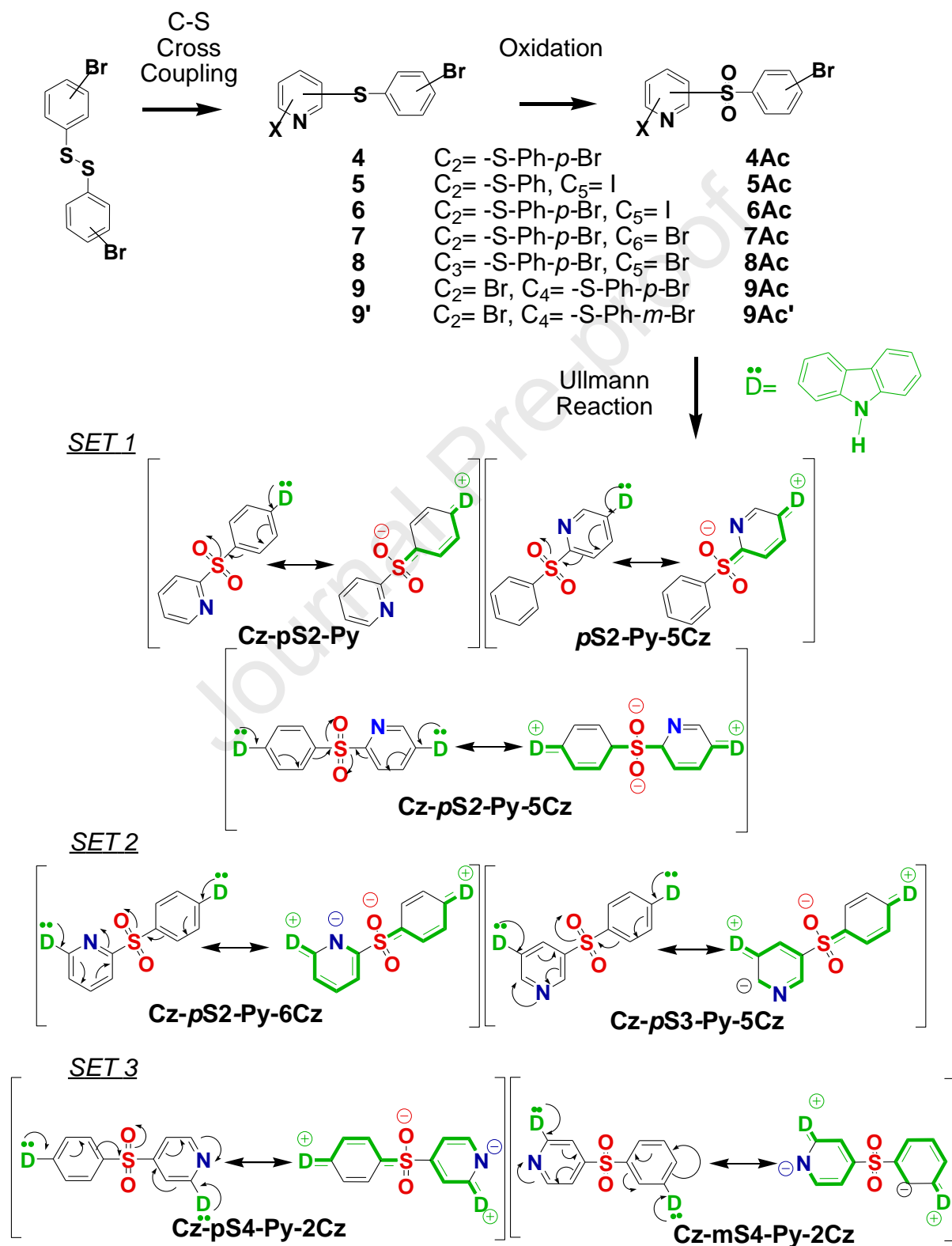
Author contributions
G.H., G.H. and F.T. synthesized the materials and performed the chemical analysis. S.G. performed the theoretical calculations. M.A. performed all photophysical measurements. M.A. and A.D. analyzed the photophysical data. A.P.M. help to interpret the data. G.H , F.T., M.A. and A.D. prepared the manuscript. All authors have given approval to the final version of the manuscript.
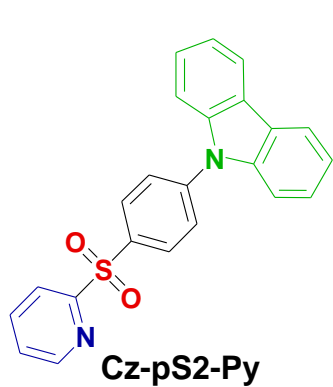
Graphical abstract

Effects of asymmetric acceptor and donor positioning in deep blue pyridyl-sulfonyl based TADF emitters

Gulcin Haykir,[a,b] Murat Aydemir,[c,d] Andrew Danos,[d] Selcuk Gumus,[e] Gurkan Hizal,[b] Andrew P. Monkman[d] and Figen Turksoy [a*]

Cz-pS2-Py

Far: D-Aa

pS2-Py-5Cz

Near: D-aA

Cz-pS2-Py-5Cz

Both: D-Aa-D

Cz-pS2-Py-6Cz

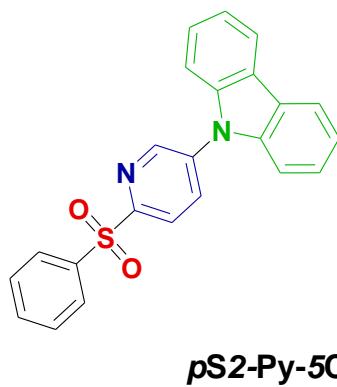**Cz-pS3-Py-5Cz**

Cz-pS4-Py-2Cz

Cz-mS4-Py-2Cz

Effects of Asymmetric Acceptor and Donor Positioning in Deep Blue Pyridyl-Sulfonyl based TADF Emitters

Gulcin Haykir,[a,b] Murat Aydemir,[c,d]* Andrew Danos,[d] Selcuk Gumus,[e] Gurkan Hizal,[b] Andrew P. Monkman[d] and Figen Turksoy [a]*
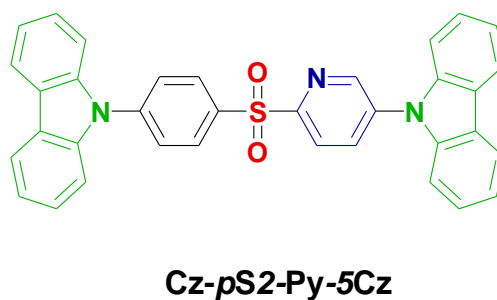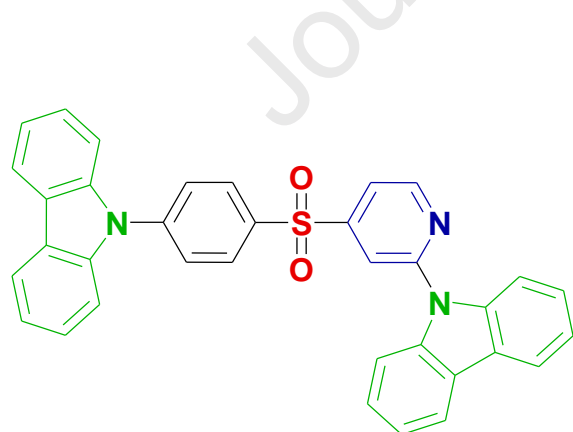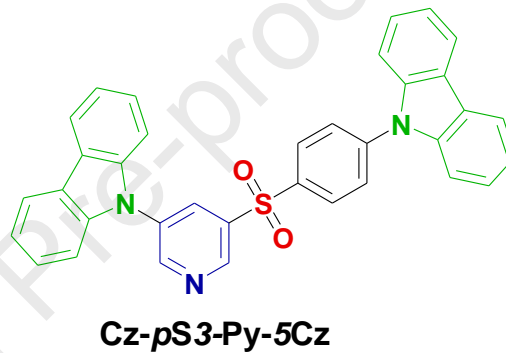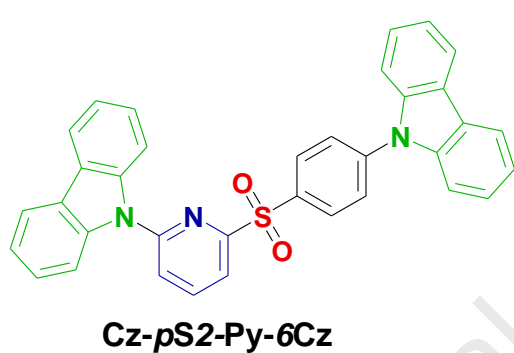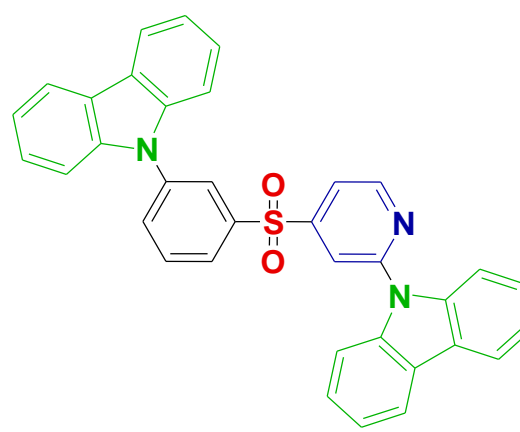
[a]TUBITAK Marmara Research Center, Institute of Chemical Technology, p.b. 21, 41470, Gebze,Turkey
[b] Department of Chemistry, Istanbul Technical University, Maslak, 34469, Istanbul, Turkey
[c] Department of Fundamental Sciences, Faculty of Science, Erzurum Technical University, Erzurum, Turkey
[d] Physics Department, OEM Research Group, Durham University, Rochester Building, South Road, DH1 3LE County Durham, United Kingdom
[e] Van Yuzuncu Yil University, Department of Chemistry, Van, Turkey

Abstract:

In this work, we report synthesis and photophysical properties of deep-blue emitting donor-acceptor (D-A) and donor-acceptor-donor (D-A-D) thermally activated delayed fluorescence (TADF) molecules using carbazole as a donor (**D**) and a pyridyl (**a**)-sulfonyl (**A**) based bifunctional group as an acceptor. The work reveals how structural changes favor reverse intersystem crossing (rISC) by forming emissive charge transfer (CT) state, which is thoroughly investigated in different donor and asymmetric acceptor positions. Three comparison sets of regioisomers are investigated. 2,5-substituted pyridine derivatives in Set-1 are D-Aa, D-aA, and D-Aa-D structures with asymmetric acceptor systems, revealing that the donor nearer to the pyridine group substantially controls the TADF properties. In Set-2, modified the D-Aa-D structures reveal how *ortho* and *meta* positioned ***a*** relative to ***A*** (keeping the carbazole at *meta* to the ***A***) affects the emission properties, deactivationg TADF and promotion triplet-triplet annihilation. In the final set, 2,4-substituted pyridyl-sulfonyl derivatives show that the positioning of the donor far from the pyridine group has minimal influence. This final set of molecules show superior optical and physical properties though, indicating the importance of correct positioning between **D**, **a**, and **A**.

Keywords: pyridyl-sulfonyl, carbazole, donor-acceptor, photoluminescence, TADF

* corresponding author

TOC

CHANGE IN STRUCTURE → EFFECT ON TADF?
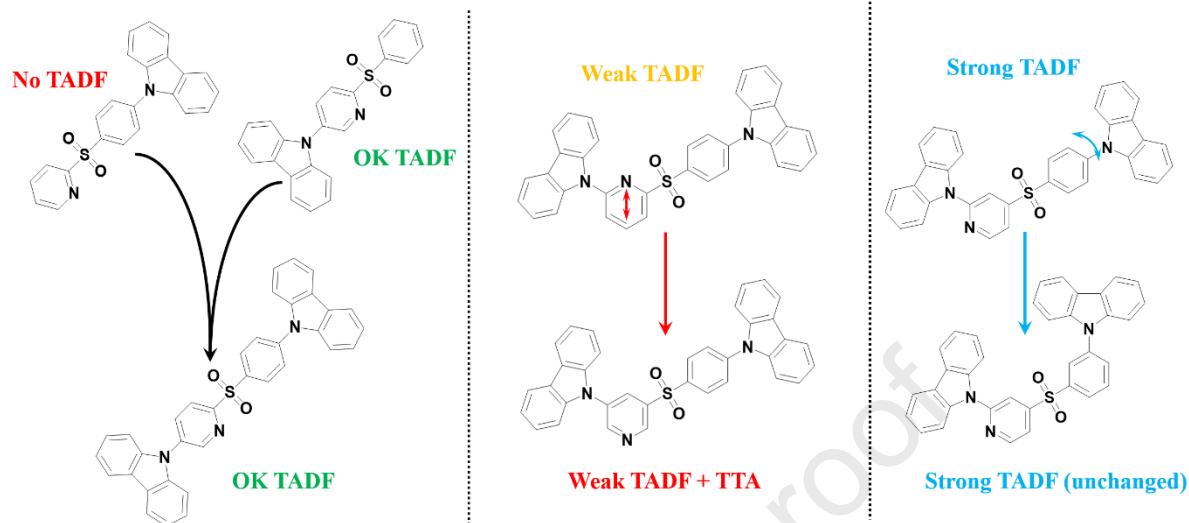
Introduction

The growing interest in state-of-the-art display applications and illumination technologies has made organic light emitting diodes (OLEDs) a very attractive field of research for the last three decades[1-3]. Driven by this, materials that emit light *via* thermally activated delayed fluorescence (TADF) have become a central feature of materials chemistry due to their ability to convert the non-emissive triplets to emissive singlet excitons by reverse intersystem crossing (rISC)[4-7]. As a result, TADF-OLEDs can attain 100% internal quantum efficiency [8] without using scarce organometallic phosphorescent emitters[9]. Additionally, heavy metal complexes have not yet produced stable deep-blue emitters suitable for applications, which is still challenging[10]. The TADF mechanism provides an alternative strategy for developing highly efficient deep-blue emitters for OLED applications[11, 12].

When designing TADF molecules, a small energy splitting is required between the excited singlet and triplet states (ΔE_{ST}) to enhance rISC and the conversion of triplets into emissive singlets. Achieving perpendicular dihedral angles between donor and acceptor units is now a common approach for designing highly efficient TADF emitters, as the energies of the resulting charge transfer (CT) singlet states can be tuned by the host environment to align localized donor or acceptor triplet states[13, 14]. Such tuning of excited states can also be achieved by modifications of donor or acceptor[11, 15] types and positions[16]. TADF molecules should also be structurally rigid to suppress non-radiative pathways to maximize the photoluminescence efficiency. Crucially, the ^{1}CT state is ideally energetically very close to a locally excited triplet state (^{3}LE) with dissimilar symmetry[17], where second-order spin-

vibronic coupling occurs between [3]LE and a charge transfer triplet excited state ([3]CT), enabling the spin flip that results in delayed [1]CT state emission[18].

Based on that approach, a small number of efficient blue TADF emitters have been designed by using, sulfone[11, 15, 19], pyrimidine[20], pyridine[21], phosphine-oxide[22], pyridine-carbonitrile[23], diazole[24], triazine[25] and their derivatives. In particular, the pyridine ring is found to have a suitably high triplet energy level and good electron withdrawing ability as an acceptor. Electron withdrawing sulfonyl groups show distorted tetrahedral geometry and restrict electron conjugation of the compounds. Carbazole is also routinely used as a donor material for blue and green TADF materials [15, 26-29] and host materials [30] .

Although pyridine and sulfone based TADF molecules have been reported by several groups, the majority of these reports focus exclusively on symmetric D-A-D materials [31, 32]. Comperatively little work has gone towards understanding the variety of possible pyridine positions and to clarify the resulting effects of photophysical properties on TADF emitters. In other TADF materials, location of the acceptor on the target molecules played a significant role in minimizing the ΔE_{ST} value and lead to well-separated highest occupied molecular orbital (HOMO) and lowest unoccupied molecular orbital (LUMO)[16, 33].

Herein, we present synthesis and photophysical properties of a series of asymmetric deep-blue emitting pyridyl-sulfonyl cored carbazole derivatives. The pyridyl-sulfonyl group is designed as an asymmetric acceptor, and carbazole groups are used as the donors in various positions. Initially with the aim of understanding the intramolecular interactions between pyridine (*a*)-sulfonyl (*A*) core and the carbazole (*D*) unit, we designed the parent molecules **Cz-*p*S2-Py, *p*S2-Py-5Cz** and **Cz-*p*S2-Py-5Cz**, with the *D* attached to the asymmetric *aA* unit on either (*D-Aa, D-aA*) or both sides (*D-Aa-D*), respectively. Comparing these materials shows that formation of charge transfer state s(CT) is significantly promoted in asymmetric (*D-aA,* 51° dihedral angle) and symmetric (*D-aA-D,* 54° -54° dihedral angle) systems, where the delayed fluorescence arise from a rISC cycle between very close energy [3]LE-[1]CT states.

The TADF properties are further investigated in two additional *D-Aa-D* comparison sets. In **Cz-*p*S2-Py-6Cz** and **Cz-*p*S3-Py-5Cz,** the nitrogen on the pyridine ring is changed from *ortho (o)* to *meta (m)* positions relative to the sulfonyl **A** (with carbazole *meta* to the sulfonyl in both). Both materials show very similar emission decay dynamics with rISC remaining operative between [3]LE-[1]CT states, although with *(m)* position nitrogen resulting in significantly reduced photoluminescence quantum yield (PLQY) and the appearance of

triplet-triplet annihilation delayed fluorescence. That gives insights into how the donor interactions with both parts of the accepting unit impact the performance.

In a final comparison, for **Cz-*p*S4-Py-2Cz** and **Cz-*m*S4-Py-2Cz,** the position of the donor on the opposite side of the pyridine is varied. Consistant with observations in the **D-Aa**, **D-aA** and **D-aA-D** materials, these comparisons show that the influence of the donor unit far from the pyridine is highly limited. Nontheless, these new structural designs give rise to very small ΔE_{S-T} values (0.01 ± 0.002 eV) and greatly enhanced PLQY values. This greatly improved performance when the two acceptor units are arranged *para* to each other is because the TADF activation mechanism is fundamentally altered compared to the parent molecules (where the formation of CT state is not promoted) and the rISC cycling therefore occurs directly between locally excited singlet-triplet states. These results therefore highlight the complexity and the potential performance gains that can be achieved by appropraite arrangement of the same donor and acceptor units.

2. Experimental details

Materials

All reagents and solvents were provided from commercial suppliers and used without further purification. Solvents were distilled by using standard methods and purged with N_2 before use. All the experiments were carried out under N_2. Column chromatography was performed on silica gel 60 (230-400 mesh) and TLC was performed on silica gel 60 F_{254} alumina plate.

General Procedure for Ullmann Reaction

Full synthetic procedures and structural charazterizations about the halogenated phenylthiopyridine (**4**, **5**, **6**, **7**, **8**, **9** & **9'**) and pyridyl-sulfonyl derivatives (**4Ac, 5Ac, 6Ac, 7Ac, 8Ac, 9Ac** & **9Ac'**) are included in Electronic Supplementary Information (ESI).

An oven-dried flask was charged with corresponding halogenated phenyl-sulfonyl pyridine derivatives (**4Ac, 5Ac, 6Ac, 7Ac, 8Ac, 9Ac and 9Ac'**) (1.0 eq), 9H-carbazole (1.1 eq for **4Ac** & **5Ac**; 2.2 eq for **6Ac, 7Ac, 8Ac, 9Ac** & **9Ac'**) and p-xylene. After then copper(I)iodide (11% of **4Ac** & **5Ac**; 22% of **6Ac, 7Ac, 8Ac, 9Ac** & **9Ac'**), 1,10-phenantroline (11% of **4Ac** & **5Ac**; 22% of **6Ac, 7Ac, 8Ac, 9Ac** & **9Ac'**) and potassium carbonate (2.0 eq for **4Ac** & **5Ac**; 4.0 eq for **6Ac, 7Ac, 8Ac, 9Ac** & **9Ac'**) were added under nitrogen atmosphere respectively. Reaction mixture was refluxed for 48 h. After cooling to room temperature mixture extracted with dichloromethane (3 x 50 mL). Combined organic phase was washed with brine and

dried over Na_2SO_4. After solvent was removed and purified with silica gel column chromatography using dichlorometane:hexane (3:1).

9-(4-(pyridin-2-ylsulfonyl)phenyl)-9H-carbazole (Cz-*p*S2-Py)

The title compound was obtained from **4Ac** (0.175 g, 0.58 mmol) as white colored target molecule **Cz-*p*S2-Py** in 54% (0.122 g).

FTIR (KBr, cm^{-1}): 3435, 1591, 1500, 1479, 1450, 1426, 1365, 1325, 1314, 1286, 1227, 1166, 1147, 1123, 1104, 1088, 1072, 1014, 990, 936, 915, 838, 790, 770, 743, 721, 679, 624, 600, 569. **^{1}H-NMR (600 MHz, CDCl$_3$)** δ_H= 8.76 (d, J=4.6, 1H), 8.37 – 8.26 (m, 3H), 8.13 (d, J=7.8, 2H), 8.00 (td, J=7.8, 1.6, 1H), 7.79 (d, J=8.5, 2H), 7.53 (ddd, J=7.6, 4.7, 0.8, 1H), 7.47 (d, J=8.2, 2H), 7.44 – 7.40 (m, 2H), 7.32 (t, J=7.4, 2H). **^{13}C-NMR (150 MHz, CDCl$_3$)** δ= 158.7, 150.6, 143.0, 139.9, 138.2, 136.9, 130.9, 127.1, 126.8, 126.3, 124.0, 122.3, 120.9, 120.5, 109.6. **HRMS (ESI) *m/z*;** [M]$^+$ 385.1012, calc. for C23H16N2O2S1 385.1005.

9-(6-(phenylsulfonyl)pyridin-3-yl)-9H-carbazole (*p*S2-Py-5Cz)

The title compound was obtained from **5Ac** (0.35 g, 1.01 mmol) as off white colored target molecule **pS2-Py-5Cz** in 90% (0.35 g).

FTIR (KBr, cm^{-1}): 3435, 3090, 3050, 1622, 1598, 1577, 1490, 1478, 1465, 1454, 1446, 1386, 1362, 1334, 1307, 1241, 1222, 1183, 1162, 1132, 1117, 1102, 1070, 1015, 998, 983, 931, 909, 863, 783, 764, 746, 717, 691, 678, 639, 613, 603, 569, 529, 513, 475. **^{1}H-NMR (600 MHz, CDCl$_3$)** δ_H= 8.97 (d, *J* = 2.4 Hz, 1H), 8.45 (d, *J* = 8.4 Hz, 1H), 8.19 – 8.15 (m, 3H), 8.13 (d, *J* = 7.7 Hz, 2H), 7.68 (t, *J* = 7.5 Hz, 1H), 7.61 (t, *J* = 7.8 Hz, 2H), 7.47 – 7.39 (m, 4H), 7.35 (ddd, *J* = 7.9, 5.7, 2.4 Hz, 2H). **^{13}C-NMR (150 MHz, CDCl$_3$)** δ= 156.2, 148.2, 139.7, 138.7, 137.8, 134.9, 134,0, 129.3, 129.1, 126.6, 124.2, 123.4, 121.5, 120.7, 109.2. **HRMS (ESI) *m/z*;** [M+Na]$^+$ 407.0822, calc. for C23H16N2O2S1Na 407.0825.

9-(4-(5-(9H-carbazol-9-yl)pyridin-2-yl-sulfonyl)phenyl)-9H carbazole (Cz-*p*S2-Py-5Cz)

The title compound was obtained from **6Ac** (0.35 g, 0.82 mmol) as white colored target molecule **Cz-*p*S2-Py-5Cz** in 47% (0.21 g).

FTIR (KBr, cm^{-1}): 3436, 3055, 2923, 1590, 1573, 1499, 1478, 1463, 1448, 1385, 1361, 1334, 1313, 1284, 1224, 1162, 1113, 1102, 1074, 1017, 929, 841, 781, 748, 723, 686, 676, 638, 623, 614, 602, 571. **^{1}H-NMR (600 MHz, CDCl$_3$)** δ_H= 9.06 (d, *J* = 2.4 Hz, 1H), 8.53 (d, *J* = 8.3 Hz, 1H), 8.41 (d, *J* = 8.5 Hz, 2H), 8.23 (dd, *J* = 8.3, 2.4 Hz, 1H), 8.14 (dd, *J* = 4.4, 3.2 Hz, 4H), 7.86 (d, *J* = 8.5 Hz, 2H), 7.53 (d, *J* = 8.2 Hz, 2H), 7.49 – 7.42 (m, 6H), 7.36 (ddd, *J*

= 16.9, 11.3, 4.2 Hz, 4H). **^{13}C-NMR (150 MHz, CDCl$_3$)** δ= 155.9, 148.3, 143.3, 139.9, 139.7, 138.0, 136.6, 134.9, 131.1, 126.9, 126.7, 126.3, 124.3, 124.0, 123.5, 121.6, 121.0, 120.7, 120.5, 109.6, 109.2. **HRMS (ESI)** *m/z*; [M+Na]$^+$ 572.1466, calc. for C35H23N3O2S1Na 572.1403.

9-(4-(6-(9H-carbazol-9-yl)pyridin-2-ylsulfonyl)phenyl)-9H-carbazole (Cz-*p*S2-Py-6Cz)

The title compound was obtained from **7Ac** (0.30 g, 0.70 mmol) as white colored target molecule **Cz-*p*S2-Py-6Cz** in 52% (0.202 g).

FTIR (KBr, cm^{-1}): 3435, 1625, 1591, 1501, 1490, 1478, 1451, 1363, 1334, 1314, 1284, 1224, 1192, 1176, 1156,1128, 1109, 1084, 1029, 992, 976, 913, 839, 810, 795, 768, 752, 721, 694, 678, 640, 622, 614, 596, 568. **^{1}H-NMR (400 MHz, CDCl$_3$)** δ$_H$= 8.41 – 8.35 (m, 2H), 8.23 (dd, *J* = 7.6, 1.1 Hz, 1H), 8.19 (t, *J* = 7.7 Hz, 1H), 8.14 (d, *J* = 7.6 Hz, 2H), 8.08 (dd, *J* = 7.6, 0.7 Hz, 2H), 7.90 (dd, *J* = 7.8, 1.2 Hz, 1H), 7.86 – 7.81 (m, 2H), 7.77 (d, *J* = 8.1 Hz, 2H), 7.46 (d, *J* = 8.1 Hz, 2H), 7.42 – 7.27 (m, 8H). **^{13}C-NMR (100 MHz, CDCl$_3$)** δ= 158.3, 152.2, 143.3, 140.5, 139.8, 138.8, 136.2, 131.4, 126.8, 126.5, 126.3, 124.7, 124.0, 121.9, 121.5, 121.0, 120.5, 120.3, 118.1, 111.3, 109.7. **HRMS (ESI)** *m/z*; [M+Na]$^+$ 572.1408, calc. for C35H23N3O2S1Na 572.1403.

9-(4-(5-(9H-carbazol-9-yl)pyridin-3-ylsulfonyl)phenyl)-9H-carbazole (Cz-*p*S3-Py-5Cz)

The title compound was obtained from **8Ac** (0.25 g, 0.663 mmol) as white colored target molecule **Cz-*p*S3-Py-5Cz** in 63% (0.23 g).

FTIR (KBr, cm^{-1}): 3435, 3052, 1591, 1500, 1479, 1451, 1424, 1360, 1326, 1334, 1315, 1220, 1194, 1147, 1101, 1082, 1020, 976, 931, 912, 843, 827, 809, 768, 748, 723, 703, 691, 678, 641, 616, 607, 569, 530. **^{1}H-NMR (400 MHz, CDCl$_3$)** δ$_H$= 9.28 (s, 1H), 9.16 (s, 1H), 8.55 (s, 1H), 8.26 (d, *J* = 8.0 Hz, 2H), 8.15 (dd, *J* = 10.9, 7.7 Hz, 4H), 7.86 (d, *J* = 7.9 Hz, 2H), 7.54 – 7.31 (m, 12H).**^{13}C-NMR (100 MHz, CDCl$_3$)** δ= 151.8, 146.2, 143.5, 139.8, 139.7, 139.4, 138.0, 135.4, 132.7, 130.0, 127.4, 126.7, 126.4, 124.2, 124.1, 121.5, 121.2, 120.8, 120.6, 109.6, 109.0. **HRMS (ESI)** *m/z*; [M+H]$^+$ 550.1661, calc. for C35H24N3O2S1 550.1584.

9-(4-(2-(9H-carbazol-9-yl)pyridin-4-ylsulfonyl)phenyl)-9H-carbazole (Cz-*p*S4-Py-2Cz)

The title compound was obtained from **9Ac** (0.2 g, 0.53 mmol) as off white colored target molecule **Cz-*p*S4-Py-2Cz** in 61% (0.177 g).

FTIR (KBr, cm^{-1}): 3435, 3039, 1591, 1576, 1500, 1489, 1479, 1465, 1449, 1406, 1362, 1329, 1314, 1284, 1274, 1244, 1226, 1193, 1154, 1120, 1100, 1078, 1028, 1015, 1004, 993, 966, 931, 914, 890, 839, 833, 794, 768, 748, 722, 707, 680, 656, 644, 620, 607, 586, 586, 563, 534, 498. **^{1}H-NMR (600 MHz, CDCl$_3$)** δ$_H$= 8.96 (d, *J* = 5.1 Hz, 1H), 8.25 (d, *J* = 8.6 Hz, 2H), 8.22 (s, 1H), 8.13 (d, *J* = 7.8 Hz, 4H), 7.92 (d, *J* = 8.3 Hz, 2H), 7.85 (d, *J* = 8.6 Hz, 2H), 7.80 (dd, *J* = 5.1, 1.3 Hz, 1H), 7.48 (t, *J* = 8.3 Hz, 4H), 7.44 – 7.29 (m, 6H). **^{13}C-NMR (150 MHz, CDCl$_3$)** δ= 153.4, 152.1, 151.2, 143.7, 139.8, 139.0, 137.3, 130.2, 127.3, 126.7, 126.4, 124.9, 124.1, 122.0, 121.2, 120.6, 120.4, 117.1, 115.4, 111.3, 109.6. **HRMS (ESI) *m/z*;** [M+H]$^+$ 550.1656, calc. for C35H24N3O2S1 550.1584.

9-(3-(2-(9H-carbazol-9-yl)pyridin-4-ylsulfonyl)phenyl)-9H-carbazole (Cz-*m*S4-Py-2Cz)

The title compound was obtained from **9Ac'** (0.24 g, 0.64 mmol) as yellowish colored target molecule **Cz-*m*S4-Py-2Cz** in 60% (0.21 g).

FTIR (KBr, cm^{-1}): 3056, 2925, 1594, 1574, 1491, 1477, 1465, 1445, 1405, 1361, 1329, 1312, 1274, 1222, 1183, 1148, 1097, 1075, 1029, 994, 968, 916, 895, 843, 794, 778, 745, 720, 710, 690, 655, 640, 616, 589, 562. **^{1}H-NMR (600 MHz, CDCl$_3$)** δ$_H$= 8.93 (d, *J* = 5.1 Hz, 1H), 8.27 (s, 1H), 8.18 (s, 1H), 8.14 (d, *J* = 7.7 Hz, 2H), 8.09 (t, *J* = 7.7 Hz, 3H), 7.92 (d, *J* = 8.0 Hz, 1H), 7.85 (dd, *J* = 19.3, 8.0 Hz, 3H), 7.75 (d, *J* = 5.1 Hz, 1H), 7.42 – 7.29 (m, 10H). **^{13}C-NMR (150 MHz, CDCl$_3$)** δ= 153.4, 151.8, 151.2, 141.7, 140.0, 139.5, 138.9, 132.5, 131.5, 126.7, 126.4, 126.2, 124.9, 123.8, 122.0, 120.9, 120.6, 120.4, 117.1, 115.4, 111.2, 109.2. **HRMS (ESI) *m/z*;** [M+H]$^+$ 550.1436, calc. for C35H24N3O2S1 550.1584.

3. Results and Discussion

3.1. Synthesis

The starting materials **1**, **1'** and **2** were purchased from commercial manufacturers and used without further purification. **3** and **3'** were synthesized according to the literature reports but with less product yields[34, 35]. The synthetic routes and their electronic resonance structures for the molecules; **Cz-*p*S2-Py**, ***p*S2-Py-5Cz**, **Cz-*p*S2-Py-5Cz**, **Cz-*p*S2-Py-6Cz**, **Cz-*p*S3-Py-5Cz**, **Cz-*p*S4-Py-2Cz** and **Cz-*m*S4-Py-2Cz** are outlined in Figure 1. The target molecules were obtained from using Br and I functionalized pyridyl-sulfonyl intermediates prepared by copper-catalyzed Ullmann reaction with moderate yields. The precursors **4Ac**, **5Ac**, **6Ac**, **7Ac**, **8Ac**, **9Ac** and **9Ac'** were synthesized from the oxidation reactions of halogenated phenylthiopyridine derivatives which had similar yields regardless of whether the substition was at *ortho*, *meta* and *para* position as **7Ac**, **8Ac** and **9Ac**, respectively.

Commercially avaliable in different positioned halopyridine molecules were reacted with **3** and **3'** to afford phenylthiopyridine derivatives **4**, **5**, **6**, **7**, **8**, **9** and **9'** with modarate yields. The more remarkable observation was that the highest yield C-S coupling reactions amongst 2,4-, 2,6-, 3,5- and 2,5- substituted pyridines which was positioned 2,4-. They were obtained from ligand free copper (I) catalyzed C(Aryl)-S coupling reactions preferentially occured at one carbon center (C4, C2, C2/C6 and C3/C5) on pyridine ring. Nucleophilic Aromatic Substitution (SNAr) Reactions of halo-pyridine derivatives are expected react with nucleophiles faster at C4 than at C2/C6 position which are depended on nucleophile types[36]. Especially soft nucleophiles such as thiolates readily undergo SnAr reactions at *para* positions (C4) of halo-pyridines[37, 38]. Nevertheless the place where the sulphur atom was attached at C2 or C4 position on pyridine can be clarifed by using NMR spectrums of different positioned other pyridyl-sulfonyl isomers. When compherensively discussed with compounds **4Ac**, **5Ac**, **6Ac**, **7Ac** and **8Ac** chemical shifts of carbon atoms on pyridine ring, they were assigned unequivocally which carbon atoms bonded with sulphur, halogen or hydrogen atoms. Especially ^{13}CNMR of **4Ac** showed that C2-(Sulphur) atom (158.5 ppm) has the most downfielded shifted signal when compared to C2(-Bromide) atom (142.5 ppm) of 2,4-dibromopyridine and C2-(Hydrogen) atom (149.9 ppm) of pyridine[39, 40]. Also the most deshielded signal of other compounds (**5Ac**, **6Ac**, **7Ac**) are 157.8, 155.1 and 158.7 ppm, respectively but the higher frequency peaks for **9Ac** and **9Ac'** have similar resonance at 151.7 ppm. As a result of all ^{13}C-NMR data analyses, Carbon-Sulphur bond formation must be placed at C4 position on pyridine ring for **9Ac** and **9Ac'**. The comparison sets were organized with their electronic resonance structures. Set 1 molecules, 2,5-substituted pyridine derivatives have the most stable electronic resonance structure and elongated π-electron conjugation. Delocalized electrons on the structures can reach at the the most electron withdrawing atom, Oxygene. For set 2 molecules, while carbozole π-electrons can move to sulfonyl oxygene on the phenyl ring, pyridine π-electrons can not. However **Cz-pS2-Py-6Cz** has more stable resonance form, due to the nitrogen atom in the pyridine ring bears a negative charge. Comparison set 3, like as set 2, pyridine π-electrons can not reach at acceptor (A) unit but electron density distrubition on the structure is more comfortable compared to **Cz-pS2-Py-6Cz** because of its sulfonyl group leads to steric effect. On the other hand donor delocalized electrons on the phenyl ring is blocked by *meta* positioned carbazole moity of **Cz-mS4-Py-**2Cz. For this 2,4-substituted pyridine derivative, π-electron movement is restricted for both side.

The compound of **Cz-*p*S2-Py**, ***p*S2-Py-5Cz**, **Cz-*p*S2-Py-5Cz**, **Cz-*p*S2-Py-6Cz**, **Cz-*p*S3-Py-5Cz**, **Cz-*p*S4-Py-2Cz** and **Cz-*m*S4-Py-2Cz** were characterized by FTIR, NMR (^{1}H-, ^{13}C-) and HRMS, the details of which were shown in ESI.
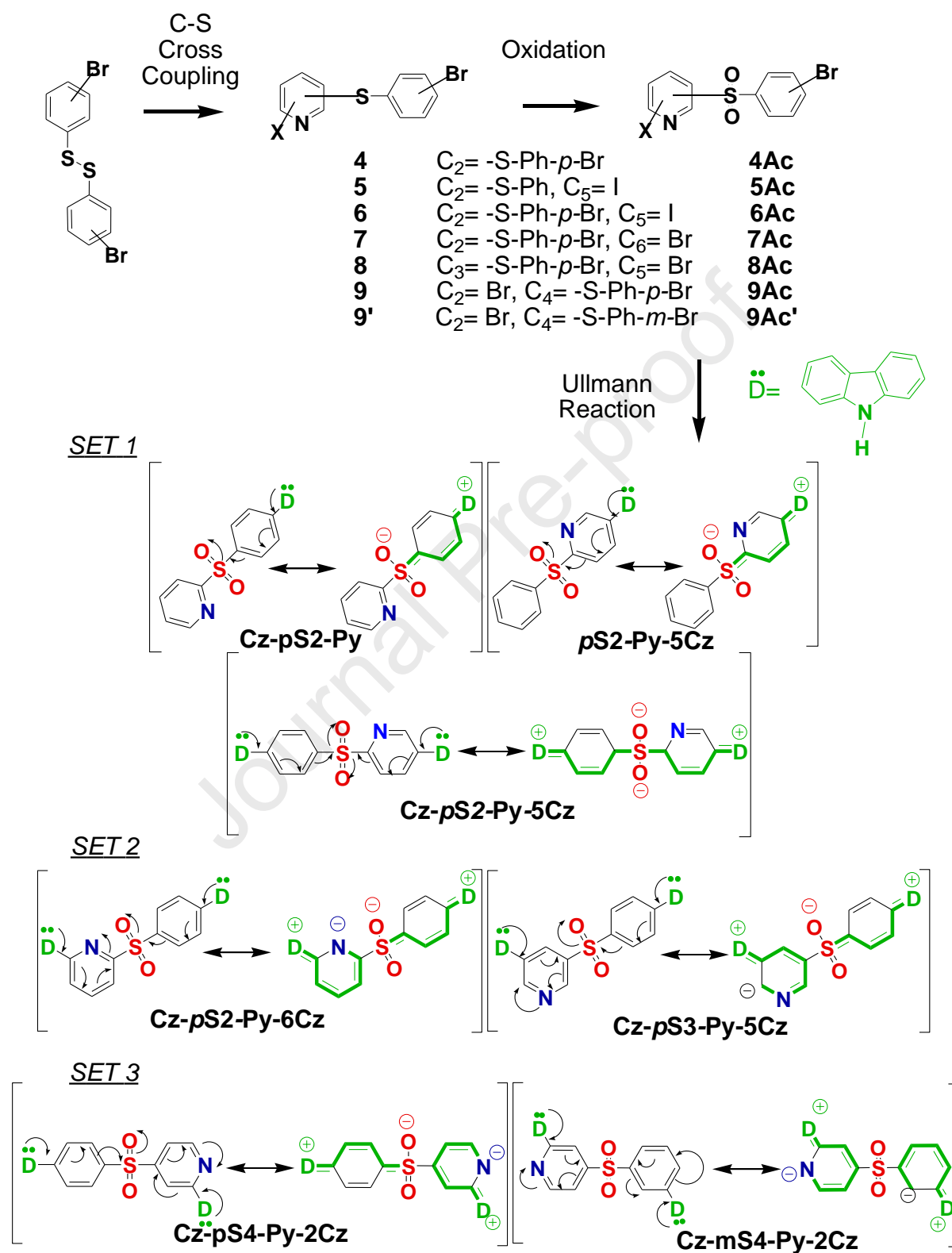
Figure 1. The synthetic route of target molecules with comparison set 1, 2 & 3.

3.2. Photophysical Properties

Ultraviolet-visible (UV-Vis) absorption and photoluminescence (PL) spectra of emitters in series of different polarity solvents (10^{-5} M concentration) are illustrated in SI-Figure 107. All molecules in the series have π-π^* transitions with some vibronic structure in 330-335 nm region. This is very similar to what was previously observed in carbazole systems[15]. Four of the molecules (pS2-Py-5Cz, Cz-pS2-Py-5Cz, Cz-pS3-Py-5Cz and Cz-pS4-Py-2Cz) have an additional shoulder at 350 nm and the appearance of the shoulder is stronger in Cz-pS4-Py-2Cz compound, indicating that the D and A are more conjugated in the ground state. All molecules show solvatochromic behavior in solution, with a red-shift in onset of emission ranging from 95-100 nm upon switching from cyclohexane to acetonitrile. In non-polar cyclohexane, vibronically structured emission is observed for all the materials, changing to unstructured and Gaussian shape emission in the more polar solvents (SI-Figure 107), which establishes predominately charge transfer (CT) character in the emissive states of the molecules.

Table 1. Photophysical properties and kinetics for the molecules in zeonex (1% wt/wt) films

Molecules	λ_{pl} (nm)	λ_{abs} (nm)	PLQY[a] (%)	S_1[b] (eV)	T_1[c] (eV)	ΔE_{ST}[d] (eV)	k_f[e] ($\times 10^7$ s^{-1})	k_{NR}[f] ($\times 10^8$ s^{-1})	k_{ISC}[e] ($\times 10^6$ s^{-1})	k_{rISC}[e] ($\times 10^3$ s^{-1})	DF/PF[g]	PF[g] (ns)	DF[g] (μs)
Cz-pS2-Py	366 [i], 465 [ii]	335	21	3.18	3.10	0.08	14	5.2	-	-	0	6.7	-
pS2-Py-5Cz	389 [i], 490 [ii]	335	30	3.20	3.18	0.02	3.9	0.9	1.6	1.0	0.015	11	420
Cz-pS2-Py-5Cz	392 [i], 489 [ii]	336	32	3.22	3.18	0.04	5.2	1.1	2.4	3.9	0.019	8.1	130
Cz-pS2-Py-6Cz	398 [i], 487 [ii]	329	9.8	3.37	3.18	0.19	4.5	4.1	2.3	34	0.03	7.0	58
Cz-pS3-Py-5Cz	396 [i], 490 [ii]	335	3.7	3.37	3.18	0.19	5.6	14	11	21	0.21	9.4	36
Cz-pS4-	419 [i],	336	42	3.21	3.20	0.01	2.0	0.3	40	9.9	1.29	12	280

Py-2Cz	507 [ii]												
Cz-*m*S4-Py-2Cz	430 [i], 510 [ii]	327	54	3.18	3.16	0.01	2.5	0.2	36	5.3	0.84	13	110

(i) in cyclohexane

(ii) in acetonitrile

[a] **Measured in zeonex film under nitrogen atmosphere**

[b] **S_1 from singlet PL onset**

[c] **T_1 from triplet PH onset**

[d] **$\Delta E_{ST} = S_1 - T_1$**

[e] **k_f, k_{ISC}, k_{rISC} from kinetic fitting of decays [41]**

[f] **k_{NR} from fitting of other kinetic rates to measured PLQY value [42]**
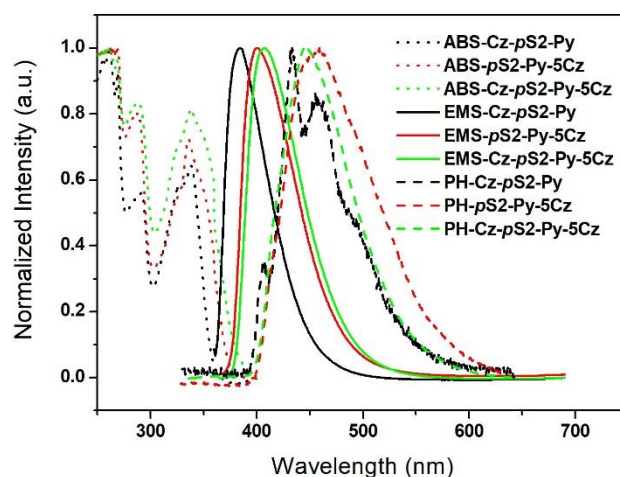
[g] **PF and DF decay rates from weighted average of biexponential fitting of decay regions, with DF/PF ratio from areas of fitted exponentials**

Time-resolved photoluminescence

Comparison set 1 (Cz-*p*S2-Py, *p*S2Py-5Cz and Cz-*p*S2-Py-5Cz)

Cz-pS2-Py   ***p*S2-Py-*5*Cz**   **Cz-*p*S2-Py-*5*Cz**

Far: D-Aa   Near: D-aA   Both: D-Aa-D
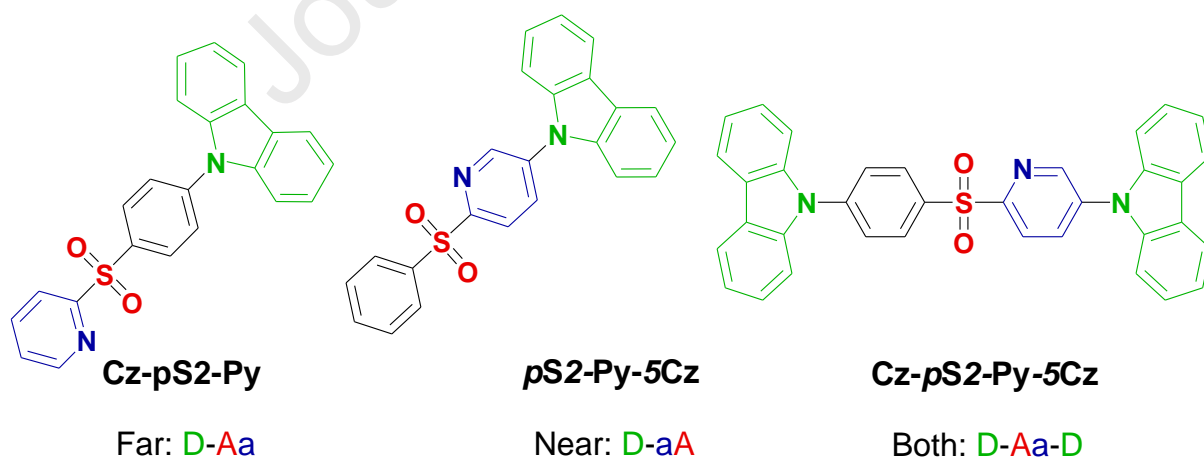
Figure 2. Normalized Uv-Vis absorption and photoluminescence spectra of **Cz-*p*S2-Py**, ***p*S2Py-5Cz** and **Cz-*p*S2-Py-5Cz** molecules in 1% w/w zeonex films at RT. Phosphorescence spectra of 1% w/w zeonex films at 80 K at >50 ms delay after pulsed excitation.

The photophysical properties of these differently connected **D-Aa** and **D-aA(-D)** materials (**D=** carbazole, **A=**sulfonyl, **a=**pyridine) were investigated in nonpolar polymer host zeonex (1% w/w, Figure 2), in which the steady-state emission spectra appears featureless and peak at 384, 400 and 405 nm for **Cz-*p*S2-Py**, ***p*S2Py-5Cz**, **Cz-*p*S2-Py-5Cz**, respectively. This immediately shows that the CT energy is lower in the **D-aA** and **D-aA-D** materials, a result of closer interactions between a carbazole and the pyridine group. Surprisingly, this also indicates that the properties of the **D-aA-D** material are dominated by the **D-aA** side of it, with the distant carbazole (as in the **D-Aa** material) having little influence. The photoluminescence quantum yield (PLQY) values are given in Table 1, where 0.21, 0.3 and 0.32 were obtained for the same comparison set order. The similarities between the PLQYs of the **D-aA** and **D-aA-D** materials are again apparent, and in contrast to the **D-Aa**.

Figure 3 shows the time-dependent emission decay curves of **Cz-*p*S2-Py**, ***p*S2Py-5Cz**, **Cz-*p*S2-Py-5Cz** materials in 1% w/w zeonex host films at room temperature (RT) and 80K, where the emission were collected from the early prompt fluorescence (PF) to the end of the delayed fluorescence (DF). The curves were obtained with 355 nm excitation (~100 µJ) in oxygen free environment. With the exception of **Cz-*p*S2-Py**, the decay curves show clear bi-modal- decays, assigned as the prompt and the long-lived delayed emission regions. The DF emission is suppressed at 80K, which is a strong indication of a TADF emission mechanism. Instead, PF is followed by an interval during which emission isbelow the detection noise floor of the iCCD camera, with longer time delays (in millisecond time region)

giving rise to phosphorescence (PH) emission. Overall, the decay kinetics are consistant with the **D-aA** region of the **D-aA-D** molecule largely controlling its optical properties, with the additional distant carbazole acting only as a spectator (as opposed to it forming a weakly bound CT state in the **D-Aa** molecule, where there is no nearby carbazole acting in competition).
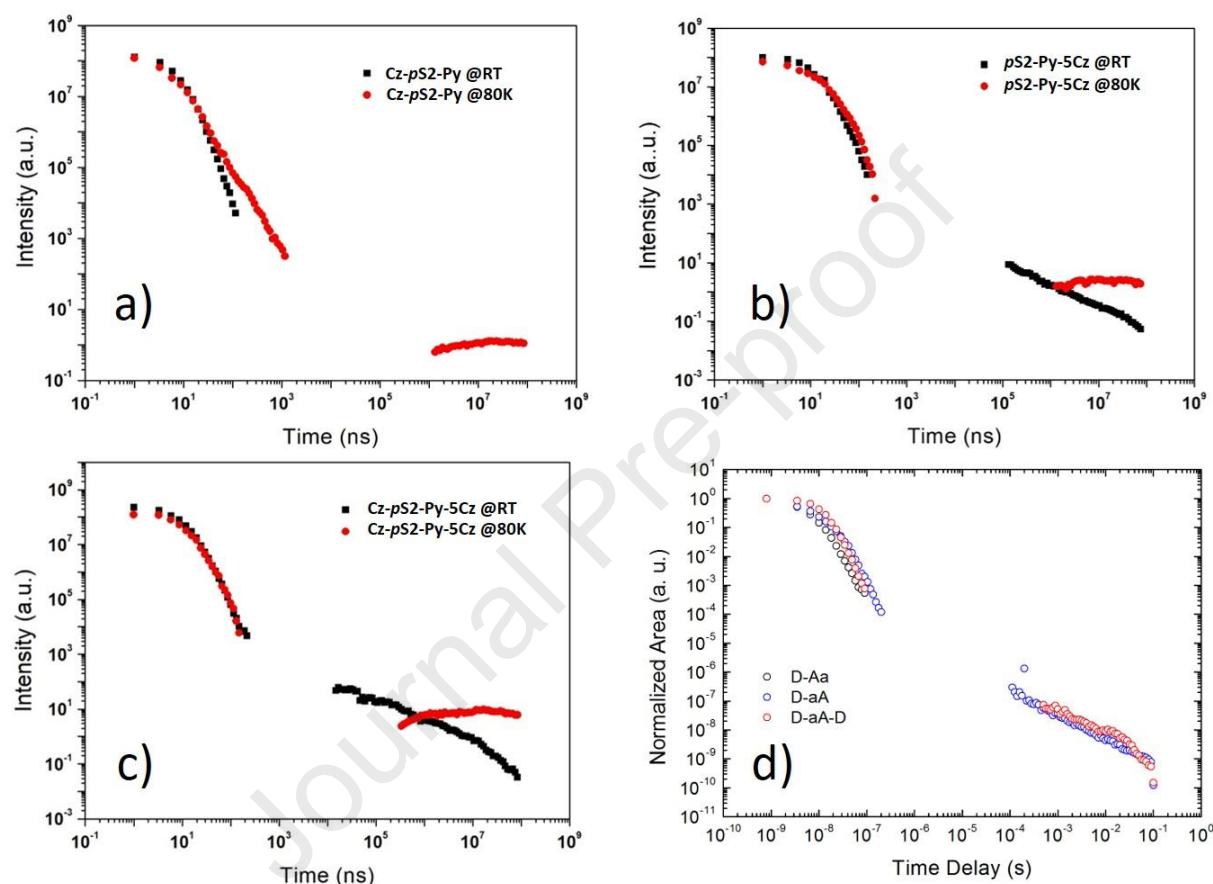
Figure 3. Emission decay kinetics of the materials in 1% w/w zeonex films at RT and 80K **a) Cz-*p*S2-Py b) *p*S2-Py-5Cz c) Cz-*p*S2-Py-5Cz,** and **d)** comparison of the decays at RT

In **Cz-*p*S2-Py** (**D-Aa** structure) a continuous dynamic red shift (~0.44 eV) is observed over the PF from delay times (TD) of 3.3 ns to 66.45 ns (Figure 4a). However, no DF is observed at longer time delays at RT (Figure 3a). At 80 K, an extended PF emission is observed (TD=115.8 ns to 1172.5 ns), which is red-shifted and Gaussian shaped spectra (Figure 5a), and perfectly matches with the emission spectra (TD=66.45 ns) at RT. This is a ^{1}CT emission and show stronger stabilization at low temperatures, therefore, having longer lifetimes. The onset value of ^{1}CT emission (3.18 ± 0.01 eV) perfectly matches with the onset value of PH emission. Although the energy splitting is nearly zero between the relaxed ^{1}CT-^{3}LE states, no DF is observed at RT. This puzzling lack of DF is likely due to the fact that the

lifetime of ^{1}CT state is very short, and is only able to undergo the strong stabilization that minimises ΔE_{ST} at low temperatures (where TADF is thermally suppressed). The fact that the steadystate PL strongly resembles the unrelaxed ^{1}CT emission further supports this interpretation of a very quickly decaying ^{1}CT state. As all three materials have very similar triplet states, the main difference in their photophysics therefore comes from different singlet states that arise from their different CT strength – itself a result of the pyridine group either being near (stronger CT, **D-aA** and **D-aA-D**) or far (weaker CT, **D-Aa**) from a participating carbazole.
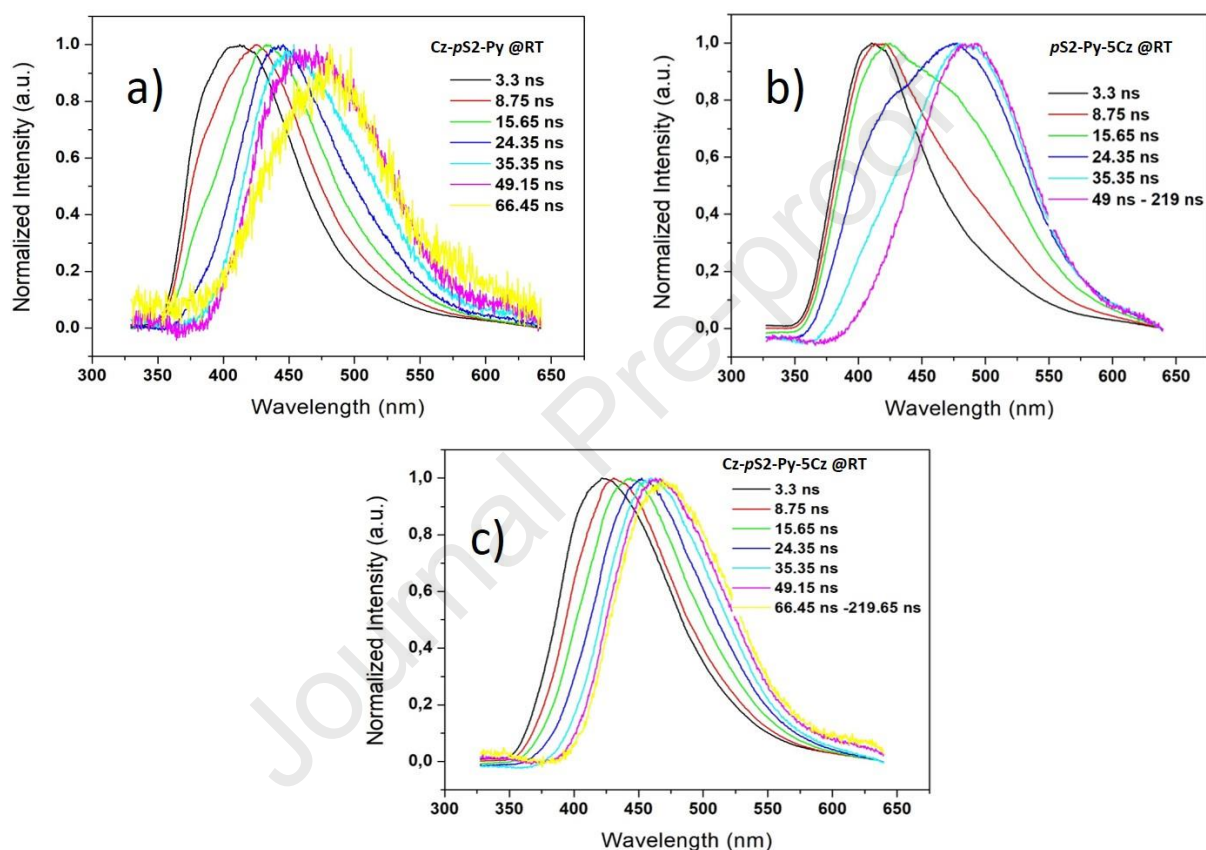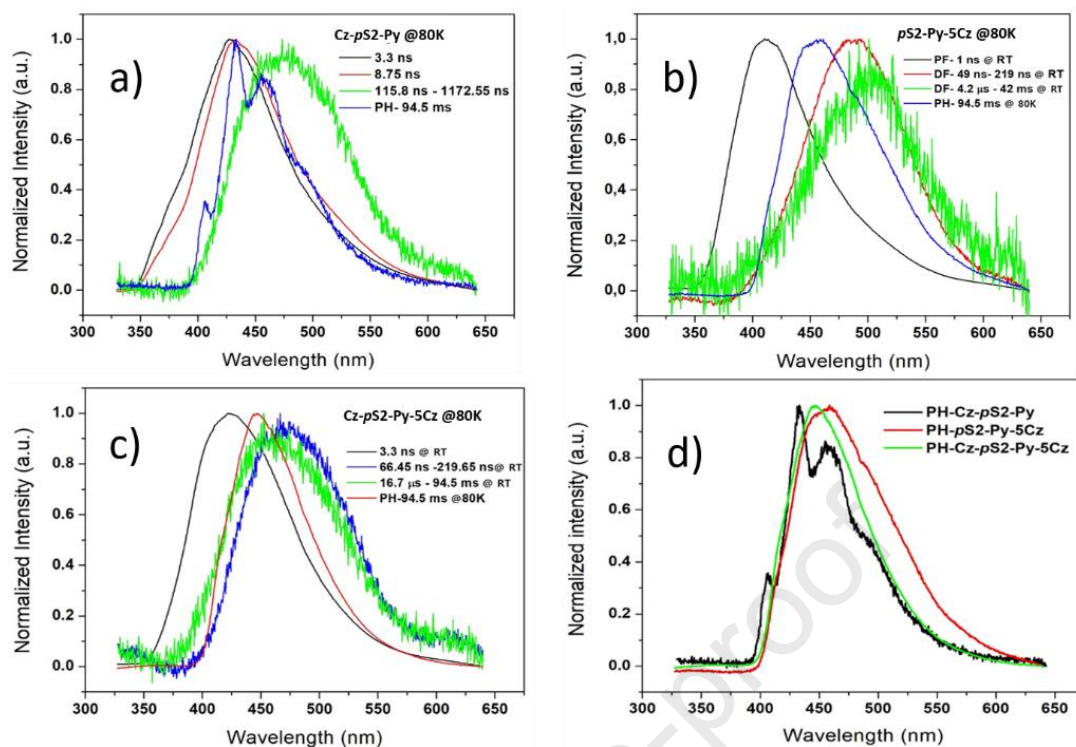

Figure 4. Time-resolved normalized emission spectra of the compounds at RT **a) Cz-pS2-Py** (TD=3.3 ns to 66.45 ns) **b) pS2-Py-5Cz** (TD=3.3 ns to 219 ns) **c) Cz-pS2-Py-5Cz** (TD=3.3 ns to 219 ns)

In **pS2-Py-5Cz**(**D-aA** structure) a continuous dynamic red shift is observed from TD= 3.3 ns to 219 ns (~0.47 eV, Figure 4b). As TD increases we observed moderate separation of the two emitting species and a clear isoemissive point is observed between ^{1}LE and ^{1}CT emissions, showing that the two emitting species are kinetically linked to each other. The PF emission (TD=3.3 ns) gradually shifts to lower energy (TD=49-219 ns) at RT. This red shift is associated with the energetic relaxation of ^{1}CT state, which stabilizes at early TD (49–219 ns) and remains constant thereafter (4.2 μs – 42 ms) at RT (Figure 5b). In this timeframe,

the emission only comes from the ^{1}CT state and the spectra have onset at 3.2 ± 0.02 eV. From TD= 1.3 ms to 75.1 ms, slightly structured PH emission is observed at 80K (Figures 2 and 5), where the energy of the ^{3}LE can be calculated from the onset of PH spectra as 3.18 ± 0.05 eV. The energy splitting between ^{1}CT and ^{3}LE was found to be 0.12 ± 0.03 eV which is sufficiently small that the ^{1}CT state can be directly populated from the ^{3}LE state at RT, leading to DF observed from ^{1}CT. As depicted in schematic excited state energy diagram (Figure 12a), the lowest energy state of **D-aA** molecule is ^{3}LE state so moderate contribution (but stringer than D-Aa) comes from ^{3}LE state to ^{1}CT *via* TADF mechanism. At 80K, two emitting species are still observable (See SI-Figure 108), with the ^{1}LE spectra shifting to ^{1}CT from TD= 1 ns to 49 ns, after which time the spectra show no further shift until TD=219 ns. At 80K the triplet states do not have enough thermal energy to cross the activation barrier to the ^{1}CT manifold, therefore no TADF is observed and ^{3}LE phosphorescence instead dominates.

As evidenced by the steadystae PL and emission decays, the **D-Aa** structure has much weaker CT state characteristic than **D-aA**, where the extra acceptor strength of a pyridine unit near to the carbazole helps to form stronger CT state. This electronic interaction is significantly weakened when the carbazole is on the other side of the molecule from the pyridine. The power dependence of DF intensity (TD=400 μs and integration time TI=70 ms) shows slope ~1 (See SI-Figure 108), indicating a monomolecular emission mechanism. TADF generally shows a slope ~1 at low and high excitation doses, while a TTA mechanism would show a slope close to 2 at low excitation doses turning to a slope ~1 at high excitation doses[43].

Figure 5. Time-resolved normalized emission spectra of **Cz-*p*S2-Py**, ***p*S2-Py-5Cz** and **Cz-*p*S2-Py-5Cz** at later delayed times **a) Cz-*p*S2-Py** spectra taken from TD=3.3 ns to 1172 ns at 80K, **b) *p*S2-Py-5Cz** spectra taken from TD=1 ns to 42 ms at RT, **c) Cz-*p*S2-Py-5Cz** spectra taken from TD=3.3 ns to 94.5 ms at RT, **d)** comparison of PH spectra at >50 ms delay time at 80K.

Finally in **Cz-*p*S2-Py-5Cz** (**D-aA-D** structure), the PF emission gradually relaxes to the DF spectrum (~0.28 eV, Figure 4c) from TD= 3.3 ns to 219 ns. This red shift is associated with the energetic relaxation of ^{1}CT state, which stabilizes between 66.45 ns – 94.5 ms at RT (Figure 5c). The DF spectrum is blue-shifted compared to **D-aA** DF spectrum, which may be the result of slightly weakened acceptor strength of the sulfonyl group due to the electron donating ability of the additional carabazole group. In this timeframe, the DF emission only comes from ^{1}CT state and the spectra have onset at 3.22 ± 0.05 eV for TD=66.45 ns. After (TD= 16.6 µs) the spectra show no further shift until TD=94.5 ms at RT. From TD= 335.5 µs to 94.5 ms, very weak PH emission is observed at 80K, where the ^{3}LE energy calculated as 3.18 ± 0.03 eV. Also, the PH spectrum of the **D-aA-D** is identical to the **D-Aa** (Figures 2 and 5d), confirming that the emissive ^{3}LE state must be localized on **D-Aa** unit. Interestingly the PH spectra is strongly structured in **Cz-*p*S2-Py** (see Figure 5d), where Cz does not participate in forming CT state; instead this is pure Cz phosphorescence. However the PH becomes broad and unstructured in other parent molecules, where the Cz interacts with acceptors and lowest triplet state takes on some CT character. This again explains why the **Cz-*p*S2-Py** material has the worst TADF. The energy splitting between ^{1}CT and ^{3}LE was

found to be nearly zero (0.04 eV, Figure 5c), and the power dependence of DF (TD=130 µs and TI=70 ms, see SI-Figure 109) shows slope ~0.95, again indicating a monomolecular DF emission process. In particular, considering the appearance of DF emission at RT and nearly zero energy gap between ^{1}CT-^{3}LE states, we can say the ^{1}CT state is significantly populated from the ^{3}LE state via TADF.

As depicted in Figure 12, the lowest energy excited singlet state of **D-aA-D** and **D-aA** molecules of ^{1}CT nature, so the DF contribution comes from spin-flip of the ^{3}LE state via TADF mechanism. The CT state associated with the **D-Aa** subgroup of the **D-Aa-D** molecule is not TADF active, as in **D-Aa** molecule. However, the decay kinetics are very similar in **D-aA** and **D-aA-D** (Figure 3d), indicating that no strong interaction occurs between the two sides of the molecule, which is consistent with our previous report on asymetrically substituted SFPC molecule[44]. Consequentially, it can be said that intramolecular interactions between the secondary acceptor (**a**=pyridine) and donor (carbazole) units play a key role on DF properties, but only when the pyridine is close enough to interact with the carbazole directly. Consequently, the effect of the secondary donor in **D-aA-D** is marginal on DF properties, and the PLQYs of the **D-aA** and **D-aA-D** are nearly identical (0.30, 0.32) while also strikingly different from the **D-Aa** (0.2)

<u>Comparison set-2</u>

<u>Cz-pS2-Py-6Cz and Cz-pS3-Py-5Cz</u>

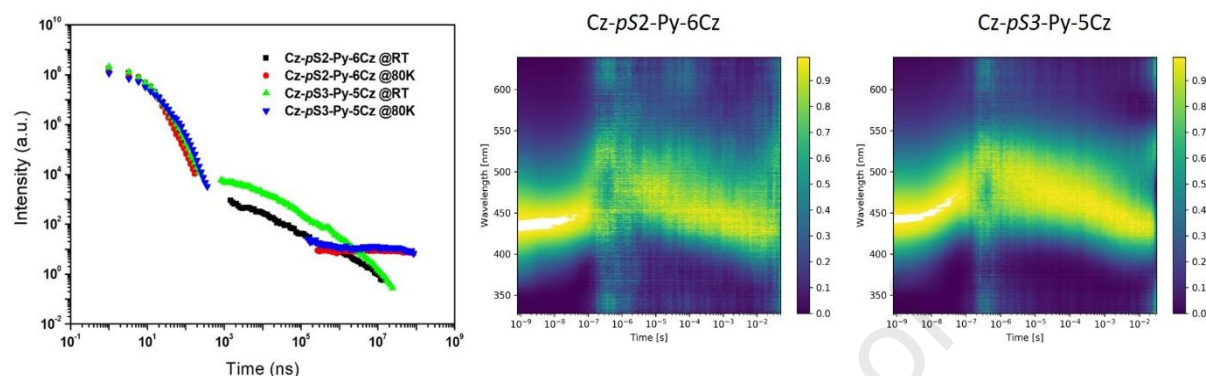**Cz-*p*S*2*-Py-*6*Cz**   **Cz-*p*S*3*-Py-*5*Cz**
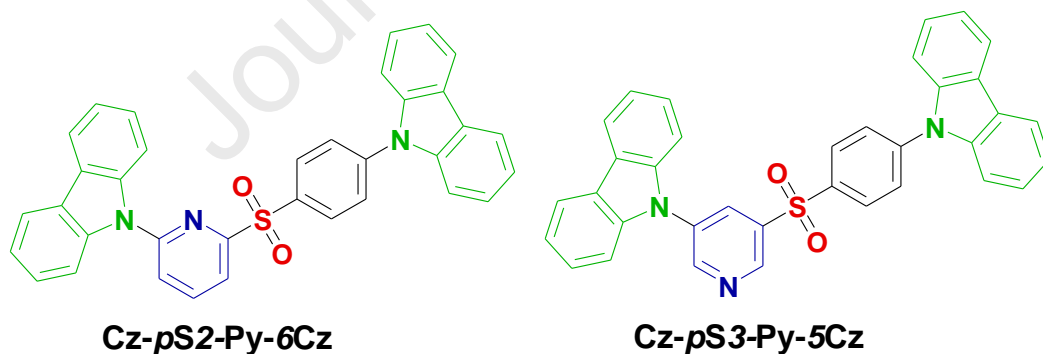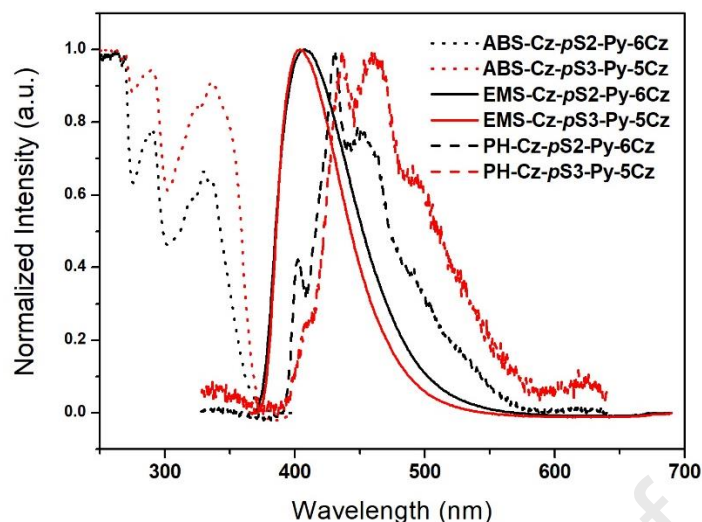
Figure 6. Normalized Uv-Vis absorption and photoluminescence spectra of **Cz-*p*S2-Py-6Cz,** and **Cz-*p*S3-Py-5Cz** molecules in 1% w/w zeonex films at RT. Phosphorescence spectra were taken at 80 K at >50ms delay after pulsed excitation.

In this comparison set, we compare the **Cz-*p*S2-Py-6Cz** and **Cz-*p*S3-Py-5Cz** molecules to get better understanding on how ***o-*** and ***m-*** positioned pyridine relative to sulfonyl group (with carbazole *meta* to the sulfonyl) effects the emission properties. Figure 6 shows the normalized steady-state absorption, emission and phosphorescence spectra of **Cz-*p*S2-Py-6Cz (D-a(o)A-D),** and **Cz-*p*S3-Py-5Cz (D-a(m)A-D)** molecules in 1% w/w zeonex film, where the emission spectra appears very identical and featureless, peaking at *ca.* 406 nm. In addition, the energy of the ^{3}LE can be calculated from the onset values of PH spectra as 3.18 ± 0.01 eV for both molecules. So, the singlet-triplet energy splittings are found as 0.19 ± 0.02 eV. Despite these similarities the PLQY values are measured as 9.8% and 3.7% for **Cz-*p*S2-Py-6Cz** and **Cz-*p*S3-Py-5Cz**, respectively. Comparing with **Cz-*p*S2-Py-5Cz** (**D(*p*)-aA-D)** of the previous comparison set, a carbazole in ***p-*** position relative to the sulfonyl group resulted in significantly enhanced PLQY(32%). In all cases the larger PLQY is accompanied by worse rISC activity, with the DF intensity (DF/PF ratio) being significantly stronger in the lower PLQY materials. This suggests that the larger PLQY values in compariosn set 1 arise not from improved rISC, but rather from less active ISC and nonradiative decay (leading to less triplet formation and more emission directly from the photoexcited singlet).

The emission decays were observed at RT and 80K (Figure 7). Both molecules show a continuous dynamic red shift from early to later time delays (Figure 8 a&b). The emission comes from a low energy CT state and dominates the both molecular systems at longer delayed times (Figure 8 c&d). It can be said that the formation of CT state is much more

favoured in **Cz-pS3-Py-5Cz** molecule than **Cz-pS2-Py-6Cz** as evidenced by the stronger PF redshift and stronger DF intensity.

Figure 7 Lifetime decays of **Cz-pS2-Py-6Cz** and **Cz-pS3-Py-5Cz** in 1% w/w zeonex films at RT and 80K.
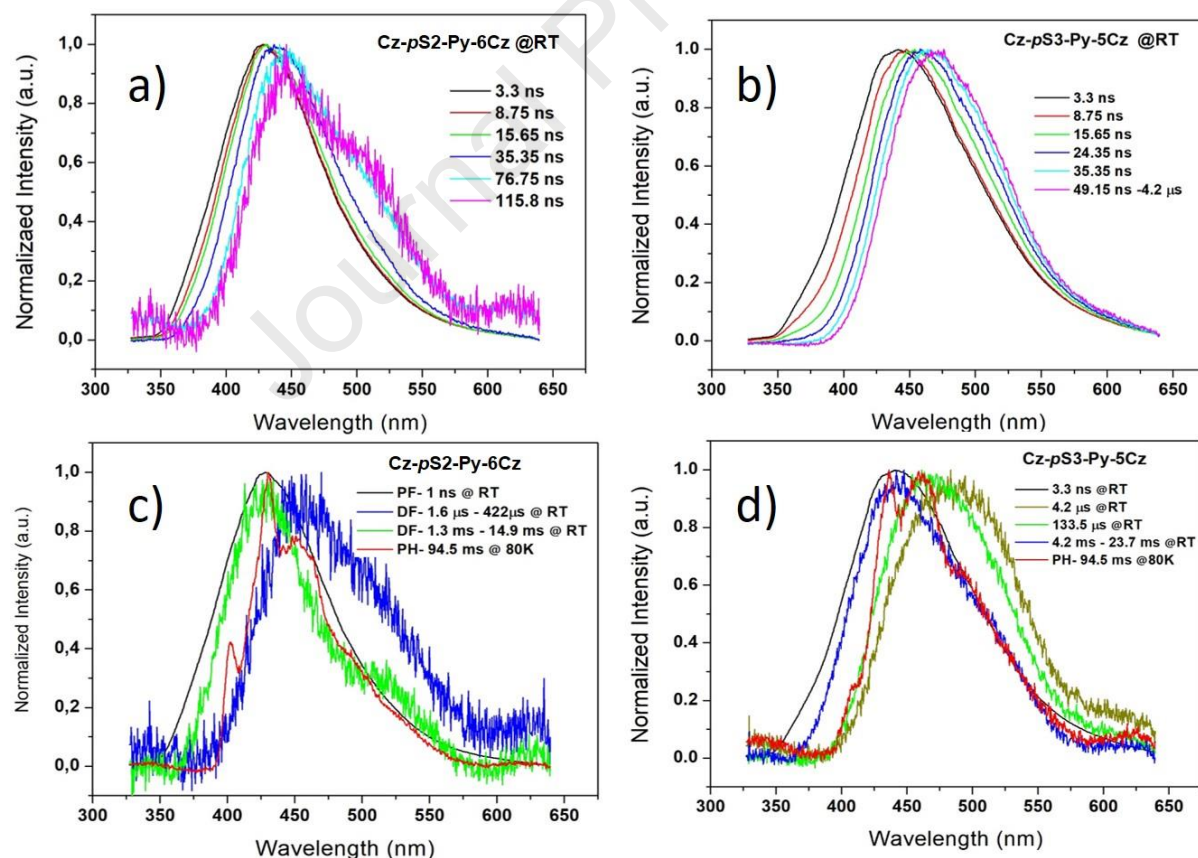
Figure 8. Time-resolved normalized emission spectra of the compounds **a) Cz-pS2-Py-6Cz** (TD=3.3 ns to 115.8 ns) **b) Cz-pS3-Py-5Cz** (TD=3.3 ns to 4.2 μs) **c) Cz-pS2-Py-6Cz** (TD=1 ns to 94.5ms) **d) Cz-pS3-Py-5Cz** (TD=3.3 ns to 94.5 ms)

After TD=1.3 ms, the DF spectra of **Cz-*p*S2-Py-6Cz** shows blue shift and emits from the exactly the same energy level of ^{1}LE at RT, which has onset at 3.45 ± 0.04 eV. After this time (TD= 1.3 ms) the spectra show no further shift until TD=14.9 ms. The intensity dependence of the DF emission was analyzed as a function of the laser excitation dose at two different time delays and integrations (TI). The power dependency of DF (TD=8 µs and TI=110 µs) shows slope 0.68 at low laser dose (≤10 µJ) and slope ~1 at high excitation doses (≤100 µJ). In the later time regime (TD=1.3 ms and TI=70 µs) the DF shows slope 1.2 (SI-Figure 110).

In **Cz-*p*S3-Py-5Cz,** the power dependency of DF (TD=2 µs and TI=10 µs) shows slope 0.97 at low and high excitation intensity doses (SI-Figure 111). However, in the longer time regime (TD=355 µs and TI=6 ms), the DF shows slope 1.4 at low laser excitation doses (≤10 µJ) and slope ~0.95 at high excitation doses (≤100 µJ). The power dependency of DF in microsecond region (~0.95) indicates a monomolecular mechanism. However, the latter power dependency confirms that an additional bimolecular triplet harvesting mechanism is also operative on DF emission, where the slope 1.4 turning from 0.95 to 1.4 is a typical behavior of TTA contribution on DF emission. A laser fluence slope between 1 and 2 indicates that TTA is not the only mechanism that results in DF at longer delayed times, but also a monomolecular triplet harvesting mechanism (TADF) makes almost equal contribution. This also helps to explain why we observe structured DF emission from ^{1}LE state at longer delayed times.

These findings indicate that the ^{1}CT state is populated from the ^{3}LE state *via* TADF, where the intersystem crossing to the triplet excited state, and reverse intersystem crossing back to the ^{1}CT state has occurred (Figure 12). Structurally, changing the nitrogen position on pyridine ring from *o-* to *m-* does not make significant difference on ^{3}LE-^{1}CT values, but, resulting in improved PLQY from the ^{1}CT state for **Cz-*p*S2-Py-6Cz**. It was previously reported that spin-orbit coupling is efficient between energetically close locally excited triplet and ^{1}CT states[45], where hyperfine coupling can in principle interconvert ^{1}CT and ^{3}CT states. The near degeneracy of the CT manifold and ^{3}LE state is crucial to promote enhanced intersystem crossing due to charge transfer spin-orbit coupling, also having very small energy gap between ^{3}LE-^{1}CT makes the ideal condition for thermally activated rISC mechanism. The DF intensity is stronger in **Cz-*p*S3-Py-5Cz**, although this is identified as partly due to additional TTA activity that is not present in **Cz-*p*S2-Py-6Cz.**

The better PLQY value in comparison set 1 material D(p)-a(o)A-D compared to analogous comparison set 2 material D(m)-a(o)A-D can only arise due to the positioning of the nearby donor carbazole. The improved PLQY is also accompanied by significantly weaker DF

though, and so cannot be due to improved rISC. As a result we instead propose that this larger PLQY is actually due to decreased ISC during the PF, consistent with weaker electronic communication between the meta-oriented donor and pyridine nitrogen. This hypothesis is supported by the fitted kinetic parameters. This lower rate of ISC leads to more efficient PF emission contributing to the overall PLQY. The more plentiful triplet states that get formed by more rapid ISC in the D(p)-a(o)A-D material are more efficiently harvested, leading to stronger DF. However this triplet harvesting is not fully efficient, leading to a lower overall PLQY.

In comparison set 2, the interaction between carbazole and pyridine is stronger in **Cz-pS2-Py-6Cz** (ortho positioning) compared to **Cz-pS3-Py-5Cz** (meta positioning). In both of these materials though the interaction between carbazole and sulfonyl is also weaker than in comparison set 1 (meta Vs para coupling). Based on the position of the donors and acceptors we would expect ISC to be stronger in **Cz-pS2-Py-6Cz**, leading to stronger DF and lower PLQY. In reality the opposite trend is observed, which we attribute to the active TTA channel in **Cz-pS3-Py-5Cz** - which gives the appearance of stronger DF, but has a fundamentally limited ability to contribute to PLQY through bi-excitonic emission processes.

Comparison set 3 Cz-*p*S4-Py-2Cz and Cz-*m*S4-Py-2Cz

Cz-*p*S4-Py-2Cz   **Cz-*m*S4-Py-2Cz**
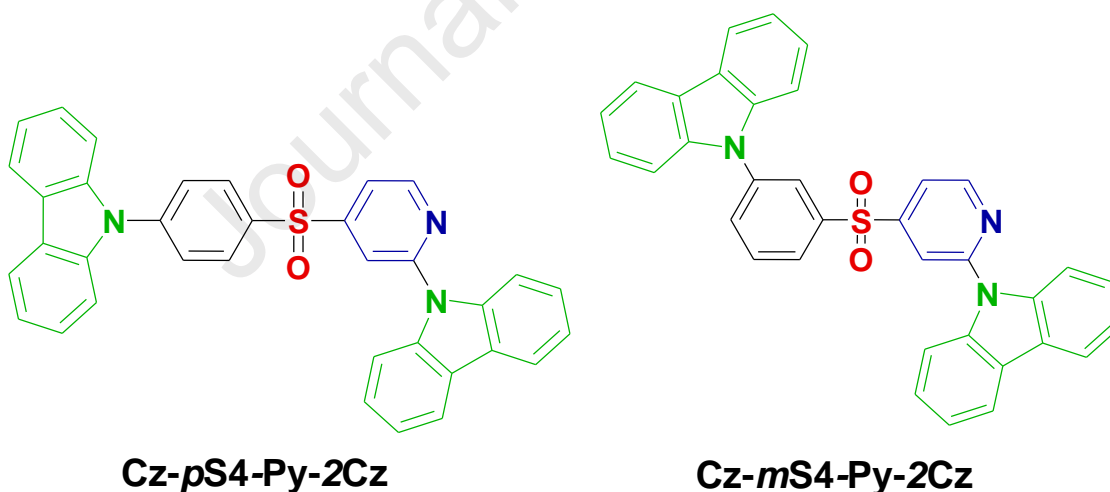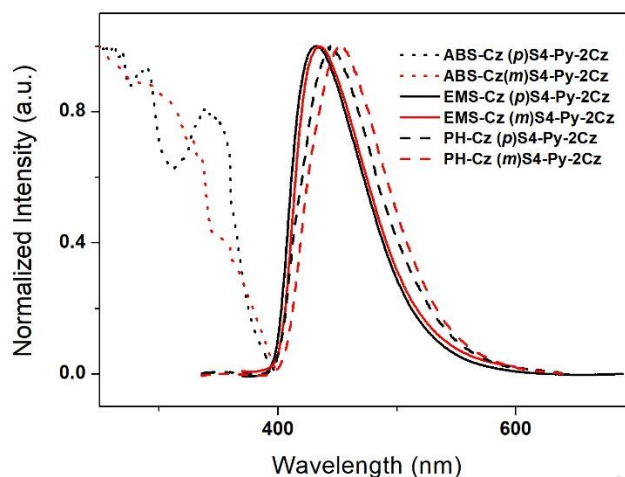
Figure 9. Normalized Uv-Vis absorption and photoluminescence spectra of **Cz-*p*S4-Py-2Cz, and Cz-*m*S4-Py-2Cz** molecules in 1% w/w zeonex films at RT. Phosphorescence spectra were taken at 80 K at >50ms delay after pulsed excitation.

In this comparison set, we compare the **Cz-*p*S4-Py-2Cz (D(*p*)-Aa-D)** and **Cz-*m*S2-Py-2Cz (D(m)-Aa-D)** molecules, where the secondary acceptor (**a**) pyridine nitrogen is in *para* position to the sulfonyl **(A),** and the far donor (carbazole) is at *m-* position to **A**. Figure 9 shows the normalized steady-state absorption, emission and phosphorescence spectra of **D(*p*)-Aa-D** and **D(m)-Aa-D** molecules in 1% w/w zeonex film,where the emission spectra appears very identical and featureless, peaking at *ca.* 432 nm. In addition, very strong PH spectra have almost the same onset values 3.20 ± 0.01 eV and 3.16 ± 0.03 eV for **D(*p*)-Aa-D** and **D(m)-Aa-D** molecules, respectively. So, the singlet-triplet energy splittings are found as 0.01 ± 0.002 eV and 0.01 ± 0.002 eV for *p*-carbazole and *m*-carbazole positioned compounds, respectively. The PLQY values are measured as 49% and 54% for **D(*p*)-Aa-D** and **D(*m*)-Aa-D**, respectively. That findings suggest that stabilising the pyridine nitrogen in *p*-position relative to the sulfonyl **A** gives the best TADF and PLQY performance. Conversely the position of the far carbazole only results in a very small impact, consistant with the presence of the **D-Aa** group having minimal influence over the overall properties of the previous **D-aA-D** material.
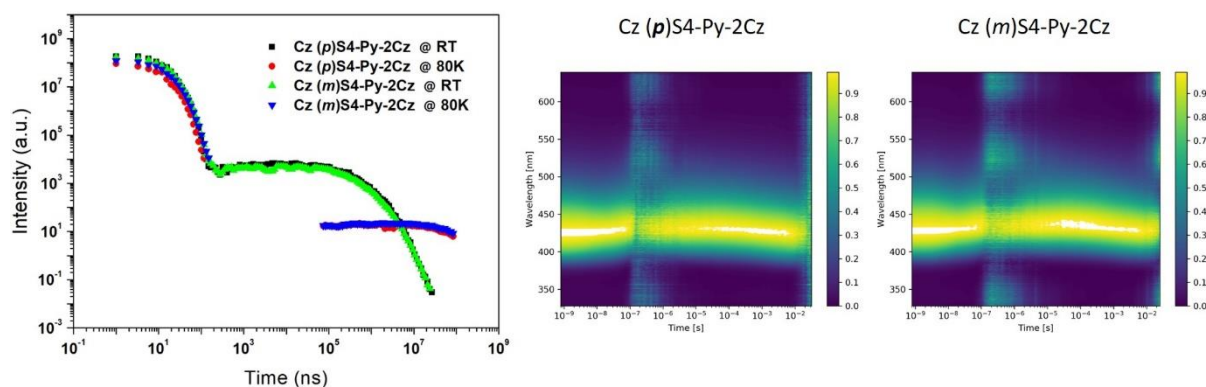
Figure 10. Lifetime decays of D(***p***)-aA-D and D(***m***)-aA-D in 1% w/w zeonex films at RT and 80K. Clearly smaller noise is observed in D(*p*)-aA-D molecule

Very similar emission decays are observed between the two materials both at RT and 80K (Figure 10). Comparing with the parent **D-aA-D** molecules above, the PF is not shifted towards the CT state neither at very early nor at longer time delays for both of the molecules (Figure 11**).**This is very different, and a remarkable feature compared with the strong tendency of [1]CT state formation and relaxation in among the other parent molecules. We attribute the increased TADF activity to the stronger electronic interactions possible between the pyridine and sulfonyl groups in *para* position, causing stronger CT character and much faster equilibration of geometry/energy – therefore no redshift in PF spectrum is observed in the nanosecond regime.

At all delay times the DF emission only comes from the [1]CT state for both molecules. As is typical for TADF molecules, the TADF is totally gone at 80K and replaced by long-lived phosphorescence. This is due to the fact that a very small ΔE_{ST} values facilitates thermally activated reverse intersystem crossing mechanism between [1]CT and [3]LE states, concomitantly DF emits from [1]CT state. (Figure 12). Perfectly linear laser fluency dependence of DF with excitation doses (SI-Figure 112) also confirms that the DF arises from rISC mechanism rather than TTA. Consequentially, we can say that ***p-*** and ***m-*** positions of carbazole unit not changes the TADF activation mechanism, where the formation of CT state is promoted above the energy of [3]LE state (different from the other molecules above), and rISC cycling directly occurs between [1]CT and very close [3]LE states (~0.01 eV).
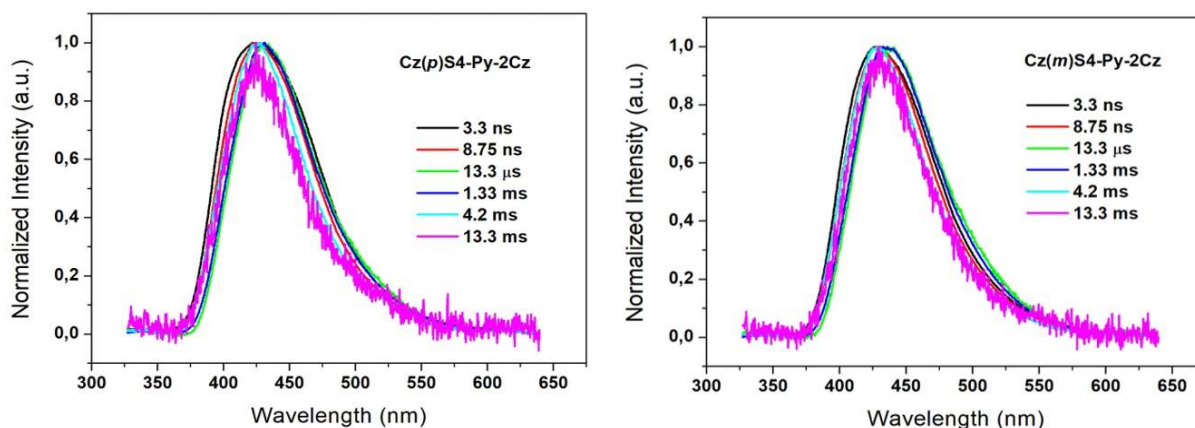
Figure 11. Time-resolved normalized emission spectra of **D(*p*)-Aa-D** and **D(*m*)-Aa-D** at TD= 3.3. ns to 13.3 ms at RT
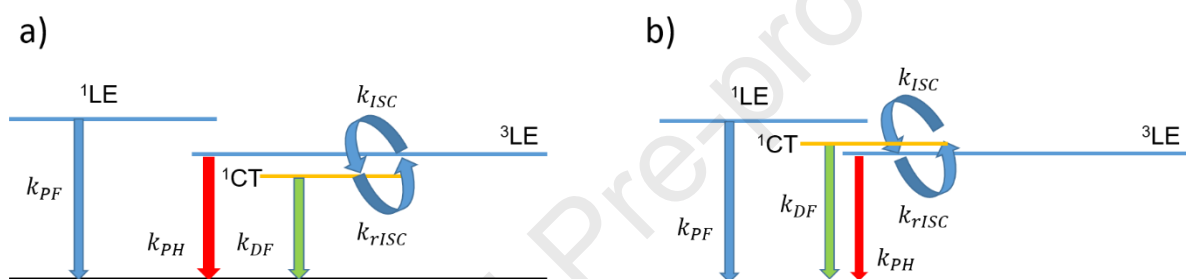
Figure 12. Schematic energy level diagram showing the electronic excited states of the molecules

3.3. Thermal Properties

The basic thermal properties of the emitters were investigated by differential scanning calorimetry (DSC) and thermal gravimetric analyzer (TGA) to identify the thermal events. The analysis data are depicted in SI Table 1. The thermal stability of all seven compounds was good, with 5% mass loss temperatures ranging from 276.1°C to 393.6°C. First comparison of compounds, **Cz-*p*S2-Py-5Cz**, ***p*S2-Py-5Cz** and **Cz-*p*S2-Py**, clearly showed that, inclusion of carbazole unit led to a raise in the melting temperature (T_m) and enhanced thermal stability. Among the compounds ***p*S2-Py-5Cz**, **Cz-*p*S2-Py**, **CzS2-Py-5Cz** and **CzS2-Py-6Cz** which sulfonyl groups placed at C2 position on pyridine, **CzS2-Py-6Cz** had the higher thermal properties. In addition, a significant correlation was found decomposition temperature that *para* isomer, **Cz-*p*S4-Py-2Cz** which had the highest T_d. When compared to *para* and *meta* isomers of 2,4-substituted derivatives, the best thermal stability belonged to *para* isomer.

3.4. Electrochemical Properties

Cyclic voltammetry (CV) was used to determine ionization potentials (IPs) of target molecules. As shown in SI Figure 106, the oxidation mechanisms and oxidation potential peaks (1), (2) & (3) were described in their CV curves. The electrochemical properties of emitters are listed in Table 2. HOMO levels of **Cz-*p*S2-Py**, ***p*S2-Py-5Cz**, **Cz-*p*S2-Py-5Cz**, **Cz-*p*S2-Py-6Cz**, **Cz-*p*S3-Py-5Cz**, **Cz-*p*S4-Py-2Cz** and **Cz-*m*S4-Py-2Cz** were determined to be 5.38 eV, 5.42 eV, 5.43 eV, 5.44 eV, 5.60 eV, 5.39 eV and 5.48 respectively, by using the energy level of ferrocene (4.8eV below the vacuum level) as an external reference and calibrating the onset potential of the first oxidation wave. Biscarbazole substituted derivatives displayed two irreversible peaks, while two quasi-reversible peaks were observed at monocarbazole substituted derivatives. Compared to molecules; longer conjugation length of 2,4-position lead to reduce oxidation potential so **Cz-*p*S4-Py-2Cz** and **Cz-*m*S4-Py-2Cz** isomers have the most narrow optical band gaps (E_g). HOMO/LUMO of **Cz-*p*S3-Py-5Cz** was deeper than other emitters due to *meta* configuration gave weak electron withdrawing ability of acceptor core.

Molecules	E^{ox}_{onset} (V)[a]	$E^{ox}_{1/2}$ (V)[a]	λ^{abs}_{onset} (nm)[b]	E_g^{opt} (eV)[b]	HOMO (eV)[c]	LUMO (eV)[c]
Cz-*p*S2-Py	1.08 [(1)]	1.18 [(2), qr] 1.43 [(3), qr]	357	3.47	-5.38	-1.91
***p*S2-Py-5Cz**	1.12 [(1)]	1.22 [(2), qr] 1.46 [(3), qr]	375	3.30	-5.42	-2.12
Cz-*p*S2-Py-5Cz	1.13 [(1)]	1.26 [(2), ir] 1.52 [(3), ir]	374	3.31	-5.43	-2.12
Cz-*p*S2-Py-6Cz	1.14 [(1)]	1.27 [(2), ir] 1.53 [(3), ir]	362	3.42	-5.44	-2.02
Cz-*p*S3-Py-5Cz	1.3 [(1)]	1.49 [(2), ir] 1.89 [(3), ir]	373	3.32	-5.60	-2.28
Cz-*p*S4-Py-2Cz	1.09 [(1)]	1.26 [(2), ir] 1.51 [(3), ir]	386	3.21	-5.39	-2.18
Cz-*m*S4-Py-2Cz	1.18 [(1)]	1.36 [(2), qr] 1.78 [(3), qr]	392	3.16	-5.48	-2.32

Table 2. The electrochemical properties of target molecules

[a] Onset oxidation potentials versus Ag/AgCl obtained from Cyclic Voltammograms for Pt electrode in contact with a 0,1 M n-Bu$_4$NF$_6$P/Acetonitrile solution of compounds relative to ferrocene; scan rate 100 mV/s.

qr and ir are referred to quasireversible and irreversible, respectively.

[b] Optical band gap (E_g^{opt}) obtained from onset of the absorption spectra by extrapolation; (E_g^{opt}=1240 / λ_{onset})

[c] The HOMO and LUMO levels were determined using the following equations; E_{HOMO} =[E_{ox} − $E_{1/2}^1$(ferrocene) + 4.8], E_{LUMO} =E_{HOMO} − E_g^{opt}.

3.5 Theoretical calculations

Gaussian 16, Revision B.01[46] package program was to obtain the ground state (S_0) geometries of all compounds with the application of B3LYP[47, 48] hybrid functional and 6-311++G(d,p) the basis set. The energies of the lowest triplet (T) and singlet excited states (S) of the compounds were obtained via Time-Dependent Density Functional Theory (TDDFT) by the same basis set.

The ground state geometries, 3-Dimensional HOMO and LUMO schemes are given in Table 3. In general, HOMO and LUMO orbitals reflect the electron donor and electron acceptor part of the structure, respectively. The computed orbital pictures clearly indicate what is expected. HOMO orbitals for all the systems were calculated to locate on carbozoles of each compound whereas pyridyl-sulfonyl moieties contribute to LUMOs (Table 3). Existance of sulfonyl group with tetrahedral geometry provided separation of HOMO and LUMO orbitals which is one of the requirements for potential semiconductors. In the energy point of view, the computed frontier molecular orbital energies and the HOMO-LUMO gap are in good agreement with the experimental data (Table 2). Moreover, measured and calculated interfrontier energy gaps are all found below 4.0 eV indicating successful design of compounds.

Both HOMO and LUMO energies lower upon changing the position of carbazole from benzene to pyridine (**Cz-*p*S2-Py** to ***p*S2-Py-5Cz**) which is due to reduction of electron donor ability of carbazole when in conjugation with electron poor pyridine. The decrease in the LUMO energy can be attributed to spread of orbital contribution to more atoms in ***p*S2-Py-5Cz**. Insertion of one more carbazole moiety restored HOMO energy in **Cz-*p*S2-Py-5Cz**. Existance of two carbazole units in **Cz-*p*S2-Py-5Cz**, **Cz-*p*S2-Py-6Cz**, **Cz-*p*S4-Py-2Cz** and **Cz-*p*S3-Py-5Cz** lead to higher LUMO energy due to loss of electron accepting ability. Only the position of the carbazole connecting to pyridine was changed among **Cz-*p*S2-Py-6Cz**, **Cz-*p*S4-Py-2Cz** and **Cz-*p*S3-Py-5Cz**. **Cz-*p*S3-Py-5Cz** possesses the lowest HOMO energy due to orbital contribution from both carbozole units. The same argument holds for **Cz-*p*S4-Py-2Cz** where the contribution of atoms to both HOMO and LUMO is least.

All the compounds considered here have been computed to have very small singlet-triplet energy difference which promote them for potential TADF structures (Table 3). Among them ***p*S2-Py-5Cz**. and **Cz-*p*S3-Py-5Cz** have the narrovest ΔE_{ST} data. When pyridine moiety is

not substituted (**Cz-*p*S2-Py**) a ΔE_{ST} value of 0.04 eV has been obtained which is quite reasonable. Among the substituted pyridines, lower ΔE_{ST} values have been computed for structures having carbazole on β position.

The singlet-triplet energy level difference of the systems are mostly effected by the conjugation throughout the structure. The disturbance of conjugation in the system results in decrease in the ΔE_{ST} values due to separation of donor and acceptor parts. The dihedral angle between donor and acceptor moieties in a potential semiconductor is quite important since it represents the degree of separation of them. In the case of TADF systems, well-separated donor and acceptor units are expected as well. The structural data were obtained after geometry optimization. Dihedral angles in Table 3 shows the degree of twisting of the donor part from planarity. The angle values out and in paranthesis are carbazole-benzene and carbazole-pyridine dihedral angles, respectively. For **Cz-*p*S2-Py** and ***p*S2-Py-5Cz**, D-A angles were computed to be 51⁰. In both cases, HOMOs were located on carbazole units as expected, but on different sides of the molecule. Angles > 50⁰ indicates disruption of the conjugation, therefore resulting in low ΔE_{ST} values. The other four systems were designed as D-A-D type with two carbazole units - one on each side. Since the higher degree of the angle represents lower overlap of HOMO and LUMO thus, smaller values, **Cz-*p*S2-Py-5Cz** and **Cz-*p*S3-Py-5Cz** were expected to be best canditates for low ΔE_{ST} values. In accordance, computational TDDFT calculations showed smallest ΔE_{ST} data for **Cz-*p*S2-Py-5Cz** and **Cz-*p*S3-Py-5Cz** which is a good representation of separation of donor and acceptor units in the systems.
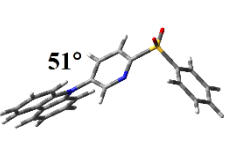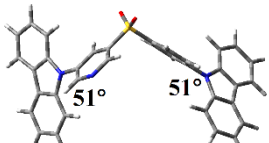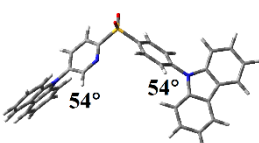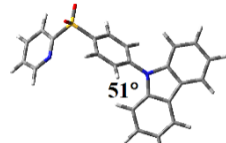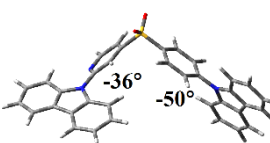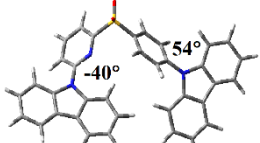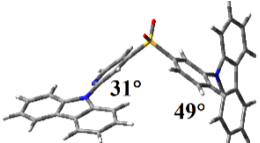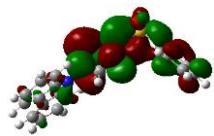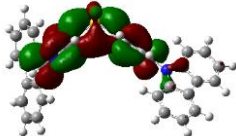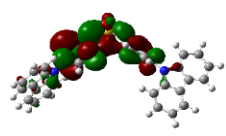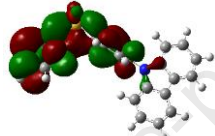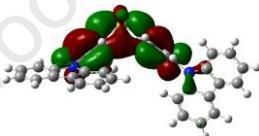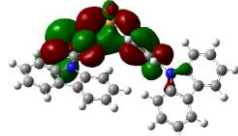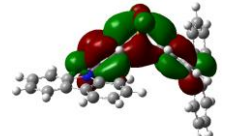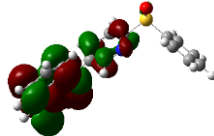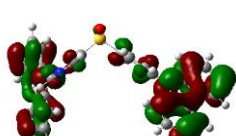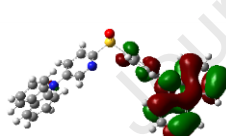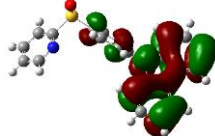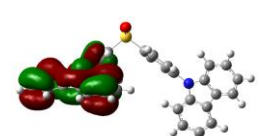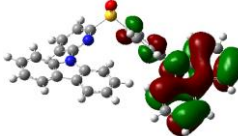
SI Figure 113 shows the 3D electrostatic potential maps for the compounds in this study which indicate the electron distribution throughout the molecule. Extreme electron localization is presented by red color whereas green or blue mean low electron density moiety. The high power electron withdrawing sulfonyl located in the center of the system is expected to pull the electrons from the donor carbazoles, which is quite represented by maps in the corresponding figure. Jang et.al reported that a uniformly distributed electrostatic potential on the acceptor side of the molecule enhances stability[49]. In the present case, non-uniform electron distribution in the parent pyridine is promoted by the connection to a high power acceptor on one side and a strong donor on the other side. Although there is still some electron localization on pyridine nitrogen, the extent of polarization is smaller that of pyridine itself. As for **Cz-*p*S4-Py-2Cz** and **Cz-*m*S2-Py-2Cz**, similar experimental TADF properties observed which is attributed to their similar theoretical structural and electronical properties. The structural difference is only on the far donor part whose effect was discussed before to be limited. Moreover, electrostatic potential maps of these duo have been computed to be almost the same. Therefore, both structural and

electronic resemblance led us expect similar TADF behavior as stated in the experimental section.

	*p*S2-Py-5Cz	Cz-*p*S3-Py-5Cz	Cz-*p*S2-Py-5Cz	Cz-*p*S2-Py	Cz-*p*S4-Py-2Cz	Cz-*p*S2-Py-6Cz	Cz-*m*S4-Py-2Cz
	51°	51° 51°	54° 54°	51°	−36° −50°	−40° 54°	31° 49°
LUMO (eV)	-2.15	-2.32	-2.22	-2.11	-2.42	-2.27	-2.49
ΔE_{ST} (eV)	0.005	0.007	0.025	0.04	0.05	0.13	0.16
HOMO (eV)	-6.22	-6.06	-5.94	-5.93	-6.03	-5.97	-6.05

Table 3. Ground state geometry (GSG), frontier molecular orbital energy diagrams (HOMO and LUMO) and dihedral angles of the compounds

4. Conclusion

Summarising, a series of deep-blue emitting TADF molecules has been rationally designed, synthesised and characterised in detail. These materials provide understanding on how to manage the positions of donors and asymetric acceptors relevant to blue OLED devices. A pyridine secondary acceptor unit was found to to manipulate the TADF properties depending on its position. The findings in **D-aA** and **D-aA-D** systems confirm that addition of donor on the opposite side of the structure makes little difference to overall emission properties, but in both systems, the formation of CT is significantly promoted, where the DF arises from a rISC cycle between very close energy ^{3}LE-^{1}CT states. In addition, the effects of nitrogen on pyridine ring were investigated in **ortho-** and **meta-**isomers, which show different acceptor strengths associated with resonance and inductive effects, resulting in different DF mechanisms and PLQY values. The best TADF and PLQY performance was found in **Cz-pS4-Py-2Cz** and **Cz-mS4-Py-2Cz** molecules, with the two acceptor groups para to each other**.** These new structural designs give rise to very reduced ΔE_{ST} values and greatly enhanced PLQY values, arising from proper arrangement of donor and acceptor(s) in the molecular structure.

References

[1]   Tang CW, Vanslyke SA. Organic electroluminescent diodes. Appl Phys Lett 1987;51:913–5. https://doi.org/10.1063/1.98799.

[2]   Burroughes JH, Bradley DDC, Brown AR, Marks RN, Mackay K, Friend RH, et al. Light-emitting diodes based on conjugated polymers. Nature 1990;347:539–41. https://doi.org/10.1038/347539a0.

[3]   Karunathilaka BSB, Balijapalli U, Senevirathne CAM, Yoshida S, Esaki Y, Goushi K, et al. Suppression of external quantum efficiency rolloff in organic light emitting diodes by scavenging triplet excitons. Nat Commun 2020;11:1–9. https://doi.org/10.1038/s41467-020-18292-0.

[4]   Dias FB. Kinetics of thermal-assisted delayed fluorescence in blue organic emitters with large singlet-triplet energy gap. Philos Trans R Soc A Math Phys Eng Sci 2015;373. https://doi.org/10.1098/rsta.2014.0447.

[5]   Graves D, Jankus V, Dias FB, Monkman A. Photophysical investigation of the thermally activated delayed emission from films of m-MTDATA:PBD exciplex. Adv Funct Mater 2014;24:2343–51. https://doi.org/10.1002/adfm.201303389.

[6]   Wu S, Aonuma M, Zhang Q, Huang S, Nakagawa T, Kuwabara K, et al. High-efficiency deep-blue organic light-emitting diodes based on a thermally activated

delayed fluorescence emitter. J Mater Chem C 2014;2:421–4.
https://doi.org/10.1039/c3tc31936a.

[7]   Zhang Q, Li B, Huang S, Nomura H, Tanaka H, Adachi C. Efficient blue organic light-
emitting diodes employing thermally activated delayed fluorescence. Nat Photonics
2014;8:326–32. https://doi.org/10.1038/nphoton.2014.12.

[8]   Dias FB, Bourdakos KN, Jankus V, Moss KC, Kamtekar KT, Bhalla V, et al. Triplet
harvesting with 100% efficiency by way of thermally activated delayed fluorescence in
charge transfer OLED emitters. Adv Mater 2013;25:3707–14.
https://doi.org/10.1002/adma.201300753.

[9]   Adachi C, Baldo MA, Thompson ME, Forrest SR. Nearly 100% internal
phosphorescence efficiency in an organic light emitting device. J Appl Phys
2001;90:5048–51. https://doi.org/10.1063/1.1409582.

[10]   Gareth Williams JA, Develay S, Rochester DL, Murphy L. Optimising the
luminescence of platinum(II) complexes and their application in organic light emitting
devices (OLEDs). Coord Chem Rev 2008;252:2596–611.
https://doi.org/10.1016/j.ccr.2008.03.014.

[11]   Stachelek P, Ward JS, Dos Santos PL, Danos A, Colella M, Haase N, et al. Molecular
Design Strategies for Color Tuning of Blue TADF Emitters. ACS Appl Mater Interfaces
2019;11:27125–33. https://doi.org/10.1021/acsami.9b06364.

[12]   Zhang X, Fuentes-Hernandez C, Zhang Y, Cooper MW, Barlow S, Marder SR, et al.
High performance blue-emitting organic light-emitting diodes from thermally activated
delayed fluorescence: A guest/host ratio study. J Appl Phys 2018;124:55501.
https://doi.org/10.1063/1.5041447.

[13]   Etherington MK, Gibson J, Higginbotham HF, Penfold TJ, Monkman AP. Revealing
the spin-vibronic coupling mechanism of thermally activated delayed fluorescence.
Nat Commun 2016;7:1–7. https://doi.org/10.1038/ncomms13680.

[14]   Dos Santos PL, Ward JS, Bryce MR, Monkman AP. Using Guest-Host Interactions to
Optimize the Efficiency of TADF OLEDs. J Phys Chem Lett 2016;7:3341–6.
https://doi.org/10.1021/acs.jpclett.6b01542.

[15]   Ward JS, Danos A, Stachelek P, Fox MA, Batsanov AS, Monkman AP, et al.
Exploiting trifluoromethyl substituents for tuning orbital character of singlet and triplet
states to increase the rate of thermally activated delayed fluorescence. Mater Chem
Front 2020;4:3602–15. https://doi.org/10.1039/d0qm00429d.

[16]   Kukhta NA, Higginbotham HF, Matulaitis T, Danos A, Bismillah AN, Haase N, et al.
Revealing resonance effects and intramolecular dipole interactions in the positional
isomers of benzonitrile-core thermally activated delayed fluorescence materials. J
Mater Chem C 2019;7:9184–94. https://doi.org/10.1039/c9tc02742d.

[17]   Gibson J, Monkman AP, Penfold TJ. The Importance of Vibronic Coupling for Efficient Reverse Intersystem Crossing in Thermally Activated Delayed Fluorescence Molecules. ChemPhysChem 2016;17:2956–61. https://doi.org/10.1002/cphc.201600662.

[18]   Dias FB, Penfold TJ, Monkman AP. Photophysics of thermally activated delayed fluorescence molecules. Methods Appl Fluoresc 2017;5:012001. https://doi.org/10.1088/2050-6120/aa537e.

[19]   Jürgensen N, Kretzschmar A, Höfle S, Freudenberg J, Bunz UHF, Hernandez-Sosa G. Sulfone-Based Deep Blue Thermally Activated Delayed Fluorescence Emitters: Solution-Processed Organic Light-Emitting Diodes with High Efficiency and Brightness. Chem Mater 2017;29:9154–61. https://doi.org/10.1021/acs.chemmater.7b02964.

[20]   Li B, Li Z, Hu T, Zhang Y, Wang Y, Yi Y, et al. Highly efficient blue organic light-emitting diodes from pyrimidine-based thermally activated delayed fluorescence emitters. J Mater Chem C 2018;6:2351–9. https://doi.org/10.1039/c7tc05746f.

[21]   Yoon SJ, Lee HJ, Lee KH, Lee JY. A study on the effect of a pyridine secondary acceptor on the emission properties of thermally activated delayed fluorescence emitters. J Mater Chem C 2020;8:7485–91. https://doi.org/10.1039/d0tc00318b.

[22]   Li C, Fan X, Han C, Xu H. A ternary phosphine oxide host featuring thermally activated delayed fluorescence for blue PHOLEDs with >20% EQE and extremely low roll-offs. J Mater Chem C 2018;6:6747–54. https://doi.org/10.1039/c8tc02010h.

[23]   Xu M, Liu M, Shi M, Ali MU, Jiao S, Cao W, et al. Efficient thermally activated delayed fluorescence based on carbonitrile-substituted pyridine and carbazole. J Mater Chem C 2019;7:13754–8. https://doi.org/10.1039/c9tc03954f.

[24]   Yang Z, Mao Z, Xie Z, Zhang Y, Liu S, Zhao J, et al. Recent advances in organic thermally activated delayed fluorescence materials. Chem Soc Rev 2017;46:915–1016. https://doi.org/10.1039/c6cs00368k.

[25]   Braveenth R, Lee H, Kim S, Raagulan K, Kim S, Kwon JH, et al. High efficiency green TADF emitters of acridine donor and triazine acceptor D-A-D structures. J Mater Chem C 2019;7:7672–80. https://doi.org/10.1039/c9tc02491c.

[26]   Lundberg P, Tsuchiya Y, Lindh EM, Tang S, Adachi C, Edman L. Thermally activated delayed fluorescence with 7% external quantum efficiency from a light-emitting electrochemical cell. Nat Commun 2019;10:1–11. https://doi.org/10.1038/s41467-019-13289-w.

[27]   Etherington MK, Kukhta NA, Higginbotham HF, Danos A, Bismillah AN, Graves DR, et al. Persistent Dimer Emission in Thermally Activated Delayed Fluorescence Materials. J Phys Chem C 2019;123:11109–17. https://doi.org/10.1021/acs.jpcc.9b01458.

[28] Colella M, Danos A, Monkman AP. Identifying the Factors That Lead to PLQY Enhancement in Diluted TADF Exciplexes Based on Carbazole Donors. J Phys Chem C 2019;123:17318–24. https://doi.org/10.1021/acs.jpcc.9b03538.

[29] Salah L, Etherington MK, Shuaib A, Danos A, Nazeer AA, Ghazal B, et al. Suppressing dimer formation by increasing conformational freedom in multi-carbazole thermally activated delayed fluorescence emitters. J Mater Chem C 2021;9:189–98. https://doi.org/10.1039/d0tc04222f.

[30] Wright IA, Danos A, Montanaro S, Batsanov AS, Monkman AP, Bryce MR. Conformational Dependence of Triplet Energies in Rotationally Hindered N- and S-Heterocyclic Dimers: New Design and Measurement Rules for High Triplet Energy OLED Host Materials. Chem - A Eur J 2021;27:6545–56. https://doi.org/10.1002/chem.202100036.

[31] Dos Santos PL, Chen D, Rajamalli P, Matulaitis T, Cordes DB, Slawin AMZ, et al. Use of Pyrimidine and Pyrazine Bridges as a Design Strategy to Improve the Performance of Thermally Activated Delayed Fluorescence Organic Light Emitting Diodes. ACS Appl Mater Interfaces 2019;11:45171–9. https://doi.org/10.1021/acsami.9b16952.

[32] Rajamalli P, Chen D, Li W, Samuel IDW, Cordes DB, Slawin AMZ, et al. Enhanced thermally activated delayed fluorescence through bridge modification in sulfone-based emitters employed in deep blue organic light-emitting diodes. J Mater Chem C 2019;7:6664–71. https://doi.org/10.1039/c9tc01498e.

[33] Jung M, Lee KH, Hong WP, Lee JY. The effect of frontier orbital distribution of the core structure on the photophysics and device performances of thermally activated delayed fluorescence emitters. J Mater Chem C 2019;7:7760–7. https://doi.org/10.1039/c9tc01577a.

[34] Natarajan P, Sharma H, Kaur M, Sharma P. Haloacid/dimethyl sulfoxide-catalyzed synthesis of symmetrical disulfides by oxidation of thiols. Tetrahedron Lett 2015;56:5578–82. https://doi.org/10.1016/j.tetlet.2015.08.041.

[35] Salehi P, Farrokhi A, Gholizadeh M. Oxidative coupling of thiols by pyridinium chlorochromate in solution and solvent free conditions. Synth Commun 2001;31:2777–81. https://doi.org/10.1081/SCC-100105325.

[36] Eicher T, Hauptmann S, Speicher A. Six-Membered Heterocycles: Sections 6.10–6.14. Chem. Heterocycles, Wiley-VCH Verlag GmbH & Co. KGaA; 2004, p. 257–310. https://doi.org/10.1002/352760183x.ch6b.

[37] Schröter S, Stock C, Bach T. Regioselective cross-coupling reactions of multiple halogenated nitrogen-, oxygen-, and sulfur-containing heterocycles. Tetrahedron 2005;61:2245–67. https://doi.org/10.1016/j.tet.2004.11.074.

[38] 2011-256116号

イリジウム錯体及びそれを用いた有機エレクトロルミネッセンス素子 - astamuse n.d. https://astamuse.com/ja/published/JP/No/2011256116 (accessed May 7, 2021).

[39] G A Pinto DC, M Santos CM, S Silva AM. Trivandrum-695 023, Kerala, India Recent Research Developments in Heterocyclic Chemistry. vol. 37. 2007.

[40] Sicre C, Alonso-Gómez JL, Cid MM. Regioselectivity in alkenyl(aryl)-heteroaryl Suzuki cross-coupling reactions of 2,4-dibromopyridine. A synthetic and mechanistic study. Tetrahedron 2006;62:11063–72. https://doi.org/10.1016/j.tet.2006.09.040.

[41] Haase N, Danos A, Pflumm C, Morherr A, Stachelek P, Mekic A, et al. Kinetic Modeling of Transient Photoluminescence from Thermally Activated Delayed Fluorescence. J Phys Chem C 2018;122:29173–9. https://doi.org/10.1021/acs.jpcc.8b11020.

[42] Haase N, Danos A, Pflumm C, Stachelek P, Brütting W, Monkman AP. Are the rates of dexter transfer in TADF hyperfluorescence systems optically accessible? Mater Horizons 2021. https://doi.org/10.1039/d0mh01666g.

[43] Kukhta NA, Matulaitis T, Volyniuk D, Ivaniuk K, Turyk P, Stakhira P, et al. Deep-Blue High-Efficiency TTA OLED Using Para- and Meta-Conjugated Cyanotriphenylbenzene and Carbazole Derivatives as Emitter and Host. J Phys Chem Lett 2017;8:6199–205. https://doi.org/10.1021/acs.jpclett.7b02867.

[44] Aydemir M, Xu S, Chen C, Bryce MR, Chi Z, Monkman AP. Photophysics of an Asymmetric Donor-Acceptor-Donor′ TADF Molecule and Reinterpretation of Aggregation-Induced TADF Emission in These Materials. J Phys Chem C 2017;121:17764–72. https://doi.org/10.1021/acs.jpcc.7b06299.

[45] Dance ZEX, Mickley SM, Wilson TM, Ricks AB, Scott AM, Ratner MA, et al. Intersystem crossing mediated by photoinduced intramolecular charge transfer: Julolidine - Anthracene molecules with perpendicular π systems. J Phys Chem A 2008;112:4194–201. https://doi.org/10.1021/jp800561g.

[46] Frisch, M.J., et al., *Gaussian 16 Rev. C.01*. 2016: Wallingford, CT. https://gaussian.com/citation/

[47] Lee C, Yang W, Parr RG. Development of the Colle-Salvetti correlation-energy formula into a functional of the electron density. Phys Rev B 1988;37:785–9. https://doi.org/10.1103/PhysRevB.37.785.

[48] Becke AD. Density-functional exchange-energy approximation with correct asymptotic behavior. Phys Rev A 1988;38:3098–100. https://doi.org/10.1103/PhysRevA.38.3098.

[49] Jang JS, Lee HL, Lee KH, Lee JY. Electrostatic potential dispersing pyrimidine-5-carbonitrile acceptor for high efficiency and long lifetime thermally activated delayed fluorescence organic light-emitting diodes. J Mater Chem C 2019;7:12695–703.

https://doi.org/10.1039/c9tc04304g.

Table Captions:

Table 1 . Maximum wavelength for absorption and emission spectra in cyclohexane *(i)* and in acetonitrile *(ii)* solution. PLQY values were recorded in 1% zeonex films under nitrogen

Molecules	λ_{pl} (nm)	λ_{abs} (nm)	PLQY (%)
Cz-*p*S2-Py	366 [i], 465 [ii]	335	21
*p*S2-Py-5Cz	389 [i], 490 [ii]	335	30
Cz-*p*S2-Py-5Cz	392 [i], 489 [ii]	336	32
Cz-*p*S2-Py-6Cz	398 [i], 487 [ii]	329	9.8
Cz-*p*S3-Py-5Cz	396 [i], 490 [ii]	335	3.7
Cz-*p*S4-Py-2Cz	419 [i], 507 [ii]	336	42
Cz-*m*S4-Py-2Cz	430 [i], 510 [ii]	327	54

Table 2. The electrochemical properties of target molecules

Molecules	E^{ox}_{onset} (V)[a]	$E^{ox}_{1/2}$ (V)[a]	λ^{abs}_{onset} (nm)[b]	E_g^{opt} (eV)[b]	HOMO (eV)[c]	LUMO (eV)[c]
Cz-*p*S2-Py	1.08 [(1)]	1.18 [(2), qr] 1.43 [(3), qr]	357	3.47	-5.38	-1.91
*p*S2-Py-5Cz	1.12 [(1)]	1.22 [(2), qr] 1.46 [(3), qr]	375	3.30	-5.42	-2.12
Cz-*p*S2-Py-5Cz	1.13 [(1)]	1.26 [(2), ir] 1.52 [(3), ir]	374	3.31	-5.43	-2.12
Cz-*p*S2-Py-6Cz	1.14 [(1)]	1.27 [(2), ir] 1.53 [(3), ir]	362	3.42	-5.44	-2.02
Cz-*p*S3-Py-5Cz	1.3 [(1)]	1.49 [(2), ir] 1.89 [(3), ir]	373	3.32	-5.60	-2.28
Cz-*p*S4-Py-2Cz	1.09 [(1)]	1.26 [(2), ir] 1.51 [(3), ir]	386	3.21	-5.39	-2.18
Cz-*m*S4-Py-2Cz	1.18 [(1)]	1.36 [(2), qr] 1.78 [(3), qr]	392	3.16	-5.48	-2.32

[a] Onset oxidation potentials versus Ag/AgCl obtained from Cyclic Voltammograms for Pt electrode in contact with a 0,1 M n-Bu$_4$NF$_6$P/Acetonitrile solution of compounds relative to ferrocene; scan rate 100 mV/s.
qr and ir are referred to quasireversible and irreversible, respectively.
[b] Optical band gap (E_g^{opt}) obtained from onset of the absorption spectra by extrapolation; (E_g^{opt}=1240 / λ_{onset})
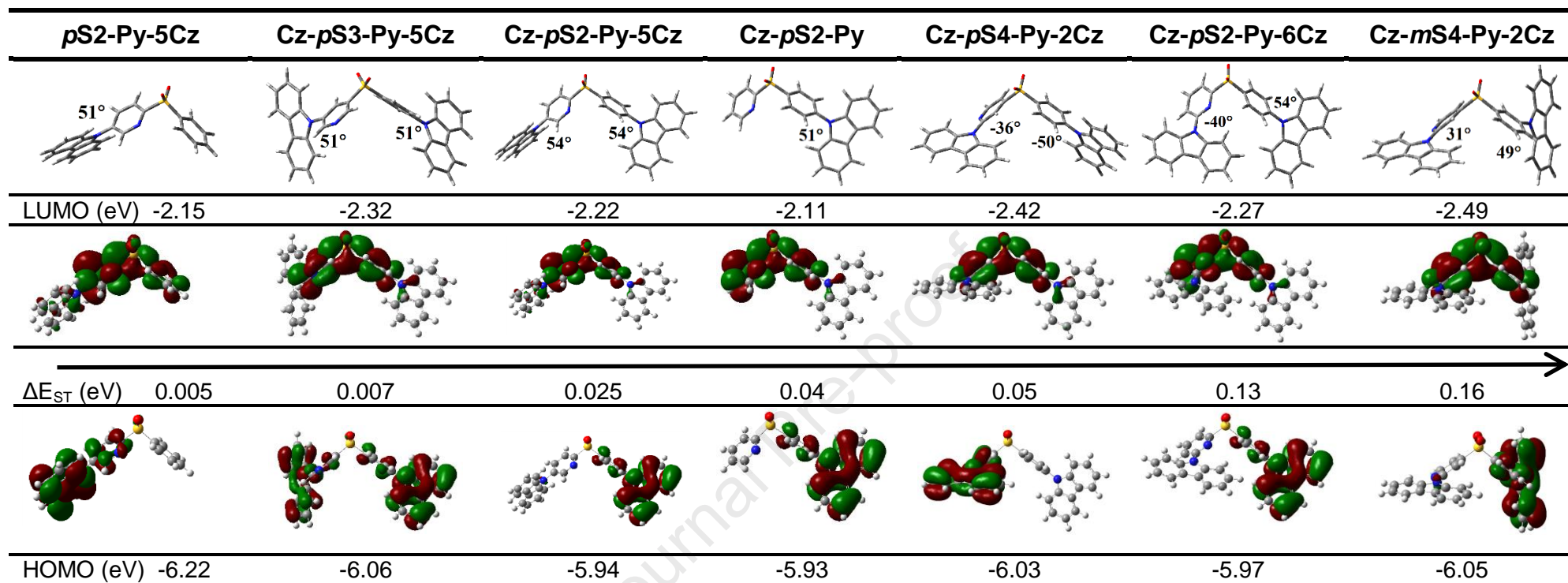[c] The HOMO and LUMO levels were determined using the following equations;
E_{HOMO} =[E_{ox} − $E_{1/2}^1$(ferrocene) + 4.8], E_{LUMO} =E_{HOMO} − E_g^{opt}.
[d] Theoretically calculated energy levels of compounds

Table 3. Ground state geometry (GSG), frontier molecular orbital energy diagrams (HOMO and LUMO) and dihedral angles of the compounds

*p*S2-Py-5Cz	Cz-*p*S3-Py-5Cz	Cz-*p*S2-Py-5Cz	Cz-*p*S2-Py	Cz-*p*S4-Py-2Cz	Cz-*p*S2-Py-6Cz	Cz-*m*S4-Py-2Cz
51°	51° 51°	54° 54°	51°	-36° -50°	-40° 54°	31° 49°
LUMO (eV) -2.15	-2.32	-2.22	-2.11	-2.42	-2.27	-2.49
ΔE$_{ST}$ (eV) 0.005	0.007	0.025	0.04	0.05	0.13	0.16
HOMO (eV) -6.22	-6.06	-5.94	-5.93	-6.03	-5.97	-6.05

Highlights:

3 different comparison sets according to their structural properties of regioisomers.

- Set-1: 2,5-substituted pyridine derivatives are categorised, which are D-Aa, D-aA and D-Aa-D type molecules and their photophysical properties in asymmetric acceptor systems shed the light on the following comparison sets.

- Set-2: we slightly modified the D-Aa-D structures as to get better understanding on how **ortho** and **meta** positioned **a** relative to *A* (keeping the carbazole at *meta* to the *A*) affects the emission properties.

- Set-3: 2,4-substituted pyridyl-sulfonyl derivatives were investigated, where the pyridyl nitrogen is in **para** position to the **A,** and the far donor (carbazole) is at **meta** position to **A**.

- Photophysical, thermal, electrochemical and computational characterizations

Dear Editor,

The authors declare no conflict of interest.

FİGEN TÜRKSOY
Dr./Chief Senior Researcher
Chemistry Institute
Barış Mah. Dr. Zeki Acar Cad. No:1 P.K. 21
41470 Gebze Kocaeli
T +90 262 677 2918
F +90 262 641 2309
www.mam.gov.tr
figen.turksoy@tubitak.gov.tr
……………………………………………………

TÜBİTAK

MAM

Declaration of interests

☒ The authors declare that they have no known competing financial interests or personal relationships that could have appeared to influence the work reported in this paper.

☐The authors declare the following financial interests/personal relationships which may be considered as potential competing interests:

There are no conflicts to declare.